

# Modeling magnetosensitive ion channels in viscoelastic environment of living cells

Igor Goychuk\*

*Institute for Physics and Astronomy, University of Potsdam,  
Karl-Liebknecht-Str. 24/25, 14476 Potsdam-Golm, Germany*

(Dated: October 5, 2015)

We propose and study a model of hypothetical magnetosensitive ionic channels which are long thought to be a possible candidate to explain the influence of weak magnetic fields on living organisms ranging from magnetotactic bacteria to fishes, birds, rats, bats and other mammals including humans. The core of the model is provided by a short chain of magnetosomes serving as a sensor which is coupled by elastic linkers to the gating elements of ion channels forming a small cluster in the cell membrane. The magnetic sensor is fixed by one end on cytoskeleton elements attached to the membrane and is exposed to viscoelastic cytosol. Its free end can reorient stochastically and subdiffusively in viscoelastic cytosol responding to external magnetic field changes and open the gates of coupled ion channels. The sensor dynamics is generally bistable due to bistability of the gates which can be in two states with probabilities which depend on the sensor orientation. For realistic parameters, it is shown that this model channel can operate in the magnetic field of Earth for a small number (5 to 7) of single-domain magnetosomes constituting the sensor rod each of which has a typical size found in magnetotactic bacteria and other organisms, or even just one sufficiently large nanoparticle of a characteristic size also found in nature. It is shown that due to viscoelasticity of medium the bistable gating dynamics generally exhibits power law and stretched exponential distributions of the residence times of the channels in their open and closed states. This provides a generic physical mechanism for explanation of the origin of such anomalous kinetics for other ionic channels whose sensors move in viscoelastic environment provided by either cytosol or biological membrane, in a quite general context, beyond the fascinating hypothesis of magnetosensitive ionic channels we explore.

PACS numbers: 87.50.C-, 05.40.-a, 05.10.Gg, 87.10.Mn

## I. INTRODUCTION

Evidences of the influence of weak electromagnetic fields including magnetic fields on many living organisms are abundant [1–9]. Most spectacular and doubtless of such manifestations are related to navigation of honeybees, fishes, birds, rats, bats, and other animals [4, 10–13] in the magnetic field of Earth of about  $B_e = 50 \mu T$  in strength. Various hypotheses related to profoundly different physical mechanisms have been suggested to explain this influence. They range from non-thermal quantum mechanisms related to spin-dependent electron transfer [4, 14], which circumvent the so-called “kT” problem [5, 8, 15], to a variety of classical mechanisms based on a widespread occurrence of biomagnetite nanoparticles in tissues of many living organisms starting from magnetotactic bacteria [16–19] and ending by the human brain [20]. Magnetite ( $Fe_3O_4$ ) has a saturation magnetization of  $M_s = 4.8 \cdot 10^5$  A/m, and elongated magnetite nanoparticles are in a single domain ferromagnetic state when their sizes range from 20 nm to 200 nm depending on the short-to-long axis aspect ratio (shape factor) [11]. Hence, magnetic energy of a spherical magnetosome (magnetic nanoparticle dressed in a lipid-protein membrane shell [17]) of the radius 100 nm with magnetic dipole moment  $\mu \approx 2$  fAm<sup>2</sup> is as large as

$E_B = \mu B_e \sim 24.5 k_B T$ , when its magnetic moment is aligned with the Earth magnetic field. The whole cells with magnetic moments in the range  $\mu \sim 4 - 100$  fAm<sup>2</sup> were identified recently as candidate magnetoreceptor cells in trout olfactory epithelium [21]. Another recent study [22] confirms the existence of cells possessing such large magnetic moments both in trouts and pigeons. However, it expresses doubts that this magnetic moment is caused by biomagnetite, and not by magnetic nanoparticles polluting environment, which are absorbed to the cell membranes. In this respect, the presence of iron-rich organelles filled by ferrihydrate in the hair cells of pigeons [22] can spell out in support of biological origin of magnetite therein, rather than on contrary. Even though the biochemical pathway of biomagnetite synthesis remains still controversial [17], the presence of ferrihydrate indirectly supports one of biochemical schemes earlier suggested [10]. Furthermore, about 10% of biomagnetite particles found in human brain [12, 20] (about  $10^6$  or even  $10^8$  per one gram of tissue in grey matter and in meninges, correspondingly, and about 50 ng/g in hippocampus on average [23]) are about or larger than 100 nm in size. In bacteria, the length of elongated magnetoparticles can reach 110 nm with shape factor 0.8 – 0.9 [18] and even larger, up to 200 nm [19]. Important is that genes encoding magnetosome specific proteins in some bacteria were identified [17]. This provides one of the strongest argumentation in the favor of biological origin of magnetite in biological cells.

Importantly, the magnitude of own magnetic field pro-

\* igoychuk@uni-potsdam.de

duced by a spherical magnetosome can reach (at peak of a highly anisotropic distribution)  $B_{\text{mag}} \sim 402$  mT near to its surface (see in Appendix A), independently of its radius. This is about  $8000\times$  larger than  $B_e$ . Thus, quantum magnetic effects can also be mediated by the magnetic near-field of a magnetosome reorienting in external magnetic field and positioned nearby an electron-transferring magneto-sensitive molecular complex, rather than directly by an external field itself [24]. The particles of intermediate size  $55 \times 44 \times 44$  nm, typical for magnetosomes met in magnetotactic bacteria [25] have  $E_B \sim 0.623 k_B T$ , and they easily make chains joined by magnetic cohesion force, being rigid enough [26] in not too strong magnetic fields, smaller than 30 mT [27]. Hence, a rod consisting of 5 such nanoparticles with magnetic moments aligned has  $E_B \sim 3.12 k_B T$ , and it can easily serve as a quite classical, compass-like sensor element for magneto-sensitive ion channels, as it will be shown in this paper. When external field becomes compatible with  $B_{\text{mag}}$  it can disrupt the magnetosome chain, or make it unstable [27]. This is why such a sensor will not work in too strong fields. It will be literally broken in pieces, presenting a disordered cluster of nanoparticles. For another typical size  $103 \times 85 \times 85$  nm also commonly met in bacteria [18],  $E_B \sim 4.23 k_B T$  for a single magnetosome. Hence, sensor can consist also of a single nanoparticle.

The idea that a magnetic nanorod can serve as a sensor and transducer of magnetic field torque has been first suggested by Yorke [28]. Kirschvink [11, 12] proposed that it can be a magnetosensitive ion channel involved with a spherical magnetosome attached to a cytoskeleton element nearby an ion channel in biological membrane and coupled by an elastic linker to the ion channel gating machinery. External magnetic field creates a torque on the magnetosome, which rotates and opens the ion channel. The sensor is considered to be essentially monostable in the Kirschvink model. This model has been refined recently for the chain of magnetosomes serving as sensor [29], but remained monostable as in the original proposal. Binhi and Chernavsky proposed a different model [24], based on bistability of magnetosome rotations induced by magnetic field for a spherical magnetosome elastically coupled to cytoskeleton. It is not related to gating of ionic channels. Rather a change in distribution of the magnetic field induced by magnetosome is of interest, in the context of a related quantum mechanism [24, 30]. Furthermore, it has been shown recently that streptavidin-linked magnetite nanoparticles of 50 nm size (in radius on average) can induce ion channel like activity being absorbed on phospholipid bilayer [31]. The corresponding ion current recordings remind somewhat the ion channel activity induced in electric fields by alamethicin peptides inserted into the membrane [32].

In this paper a further generalization of the model by Kirschvink *et al.* is suggested and studied. The generalization consists in several profound aspects. First, stochastic motion of sensor is considered to be bistable

because of bistability of ion channel gate to which the sensor is coupled. Such a bistability is a common point in describing stochastic dynamics of ionic channels [33]. To include it in the sensor dynamics we adopt a gating spring model [34] assuming that the gate can take on just two conformations, open and closed. Similar model has originally been suggested in relation to the hair cell dynamics. Second, we consider a possibility that magnetic sensor can be coupled to gates of several ionic channels making a cluster, i.e. that a compact cluster of ionic channels and a magnetic nanoparticle serving as sensor make a magneto-sensitive complex in biological membrane. This can explain why such magnetosensitive ion channels, as separate units, were not found thus far. Third, and most important in a more general context of gating stochastic dynamics of ionic channels: We consider the influence of viscoelasticity of the environment in which sensor is moving on the sensor dynamics. We show that viscoelasticity alone can result in profoundly non-exponential residence time distributions of the channels in their open and closed states such as stretched exponential distribution [35, 36] and power law distributions [35, 37–41]. This explanation of unusual gating kinetics is different from other physical theories suggested thus far which are based, in particular, on a complex free energy landscape for sensor or conformational dynamics of the whole ion channel with huge many multiply degenerated minima and maxima (glassy like dynamics) [42–44]. The latter one can be modeled in a simplest possible fashion as a continuous normal diffusion in a potential box, which already allows to explain [45] the origin of  $-3/2$  power law in the distribution of closed times [38, 39] in conjunction with the origin of Hodgkin-Huxley voltage dependence [33, 45]. Such normal diffusion can become also anomalously slow (fractional diffusion) – a modeling pathway explored in [46].

Recent work [47, 48] suggests, however, that the discussed anomalous kinetics can also result from standard bistable dynamics of sensor, commonly assumed in biophysics textbooks [33], as a result of memory effects caused by viscoelasticity of the environment. This is a very appealing and simple physical explanation indeed. In this respect, both cytosol and plasma membrane are viscoelastic [48, 49]. Hence viscoelasticity is considered as a major cause of experimentally observed anomalous diffusion in crowded colloidal and polymer solutions [50–56], and living cells [57–60], as well as in single protein molecules [61]. To study such effects, the approach of generalized Langevin equation (GLE) characterized by a power law scaling memory kernel and power law correlated thermal noise of environment, which are related by fluctuation-dissipation theorem (FDT), provides a major well-established theoretical framework in the case of linear dynamics [50, 54]. It is not easy to generalize this framework towards nonlinear dynamics in bi- and multistable potentials. For example, a corresponding *exact* Fokker-Planck description which would mirror and complement the GLE approach, like in the case of memoryless

dynamics, is simply not developed thus far for potentials other than linear and parabolic [62]. In other words, any nonlinearity creates a problem for Fokker-Planck description of such a dynamics with memory [47, 48, 63]. Recently, we bypassed such difficulties within the GLE approach using the road of multi-dimensional Markovian embedding of GLE dynamics within a generalized Maxwell-Langevin model of viscoelasticity [47, 48]. It has also been generalized to include negative correlations of stochastic force and corresponding memory effects leading to superdiffusion and supertransport [64]. The utility of this approach has been demonstrated on various basic models of nonlinear stochastic dynamics such as bistable dynamics [47], washboard dynamics [47, 48, 65], anomalous rocking ratchets [48, 66–69], anomalous flashing ratchets [70], and also in applications to molecular motor dynamics in viscoelastic cytosol [71–73].

In the context of magnetosomes dynamics in viscoelastic cytosol Kirschvink *et al.* have repeatedly taken the cytosol influence into account by enhancement of the coefficient of *normal* viscous friction experienced by magnetosome by a factor of about 100 [12, 21]. This was a standard way to think about influence of viscoelasticity and crowding in cytosol in biological applications until recently [74]. However, recent results on anomalous diffusion of nano- and submicron particles in living cells suggest that this enhancement can be much larger, of the order of 1000, and even larger [57, 71, 75], depending, in particular, on the size of particle [76]. Cytosol seem to normally operate at the edge of a phase transition from liquid-like state to a solid-like state with broken ergodicity [77]. Moreover, even for the enhancement factor 100 the bistable orientational dynamics of magnetic nanoparticles would be so slow, as we show in this paper, that it would be completely out of interest within a biological context. However, a major effect, which introduces viscoelasticity, is emergence of transient subdiffusion which is much faster than the asymptotic limit of normal diffusion. In fact, this asymptotic regime can become completely irrelevant for mesoscopic dynamics. This paradoxical fact also follows from the non-Markovian rate theory developed beyond the standard memoryless Kramers theory [78–82], see [83] for a review, and below. Namely this “much faster, not slower” [75, 84, 85], paradoxically due to subdiffusion, makes operating of such bistable magnetic sensors possible in viscoelastic cytosol. This provides one of most important results of this work, which lends a further support to the idea of magnetic field sensing with classical dynamics of sufficiently large biomagnetite nanoparticles.

## II. MODEL AND THEORY

We consider the following model. Biomagnetite rod made of a chain of magnetosomes of total length  $L$ , or a single elongated magnetic nanoparticle can rotate with one end fixed e.g. on a cytoskeleton mesh-

work attached to the cell membrane inside the cell (see Fig. 1 for an idea). It is also elastically attached to the gates of ionic channels (one is shown) by flexible linkers, which are modeled here within a finite extensible nonlinear elastic (FENE) model [86]. The channel gate or rather a molecular latch, which fixes the gate in its either open or closed state, can be in two states. The closed state is characterized by the energy  $\epsilon_1$ , and the open one has the energy  $\epsilon_2 - f_0 x$ , which depends on the linker elongation  $x$ , where  $f_0$  is a force constant characterizing the strength of coupling (force exerted by the linker on the gate). Elastic energy is  $U_{\text{FENE}}(x) = -\frac{1}{2} k l_{\text{max}}^2 \ln(1 - x^2/l_{\text{max}}^2)$  within FENE model, where  $k$  is elastic spring constant, and  $l_{\text{max}}$  is the maximal extension length of the linker, when it is fully stretched. Statistical mean force exerted by the channel gate on the linker can be found as  $f(x) = -dG(x)/dx$  from the potential of mean force  $G(x) = -k_B T \ln Z(x)$ , where  $Z(x) = \exp[-\beta \epsilon_1] + \exp[-\beta(\epsilon_2 - f_0 x)]$  is the statistical sum of gate, and  $\beta = 1/(k_B T)$  is inverse temperature. Here, one implicitly assumes that the own gate/latch dynamics (transitions between two states) is very fast, and, hence the actual gating dynamics is enslaved by the sensor dynamics and reflects the latter one. Mean force is  $f(x) = f_0 p(x)$ , where

$$p(x) = \frac{1}{1 + \exp[-f_0(x - l_0)/(k_B T)]}, \quad (1)$$

is probability of the gate to be open and  $l_0 = (\epsilon_2 - \epsilon_1)/f_0$ . In order to define some  $x_0$  as equilibrium point, we following [34] redefine mean force by a shift as  $f(x) = f_0[p(x) - p(x_0)]$ . The motion of rod is assumed to be restricted to the plane orthogonal to the membrane, and characterized by the angle  $\phi$ ,  $0 \leq \phi \leq \pi$  counted from the membrane plane in the counter-clockwise direction. The linker elongation is approximated as  $x(\phi) = 2l[\sin(\phi/2) - \sin(\phi_0/2)]$ , where  $l$  is the rotation arm, and  $\phi_0$  is an equilibrium angle. The external magnetic field  $B$  is directed at the angle  $\psi$  within the plane of motion. The potential of mean force (torque) acting on the rod in our model is

$$\begin{aligned} U(\phi) = & -\frac{1}{2} k l_{\text{max}}^2 \ln \left\{ 1 - [x(\phi)/l_{\text{max}}]^2 \right\} \\ & - k_B T m \ln \{ 1 + \exp[f_0(x(\phi) - l_0)/(k_B T)] \} \\ & + m f_0 p(\phi_0) x(\phi) - \mu B \cos(\psi - \phi), \end{aligned} \quad (2)$$

where  $p(\phi_0) = p(x = 2l \sin(\phi_0/2))$ ,  $\mu$  is the magnetic moment of the rod, and  $m$  is the number of ion channels coupled to sensor and treated in a mean-field fashion (all gates move synchronously enslaved by the same sensor). We shall scale the energy in units of  $U_0 = k l^2$ , temperature in the units of  $U_0/k_B$ , distances in units of  $l$ , and forces in units of  $f_u = U_0/l$ .  $U_0$  will be fixed to  $U_0 = 10 k_B T_r \approx 41 \text{ pN} \cdot \text{nm} \approx 0.25 \text{ eV}$ , where  $T_r$  is a typical room temperature,  $T_r \approx 297 \text{ K}$ . For a typical  $k = 0.3 \text{ pN/nm}$  [87], this corresponds to  $l \approx 11.69 \text{ nm}$  and force units  $f_u \approx 3.51 \text{ pN}$ . For the purpose of illustration, magnetic nanorod is assumed to be made of

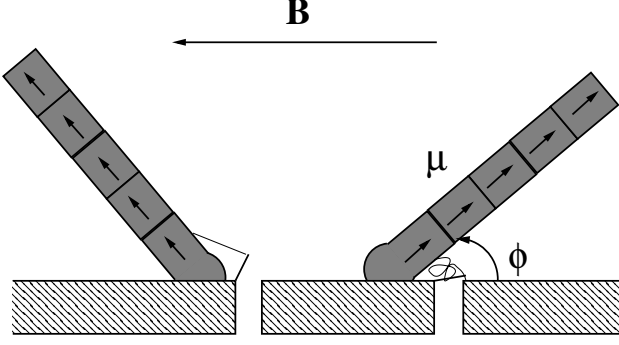


FIG. 1. Cartoon of the considered model of magnetosensitive ion channel expressing the idea. Proportions are not held. Rotation of nanorod is coupled via flexible linkers to gates of ion channels, which can form a cluster. One channel is shown for simplicity.

magnetosomes of size  $55 \times 44 \times 44 \text{ nm}^3$ . For the magnetosome core made of magnetite with saturating magnetization of  $M_s = 480 \text{ kA/m}$  its elementary magnetic moment is  $\mu_1 \approx 0.0511 \text{ fAm}^2$  and its energy in the magnetic field of Earth taken to be  $B = B_e = 50 \text{ } \mu\text{T}$  is  $\mu_1 B \approx 0.623 k_B T_r$ , when it is aligned with the field direction. The sensor can be operable already for  $n = 5$  nanoparticles in the rod with  $\mu_5 B = 5\mu_1 B \approx 3.115 k_B T_r$ , and a reliable operation can be achieved for  $n = 7$  with  $\mu_7 B = 7\mu_1 B \approx 4.363 k_B T_r$ . For these two values we shall do illustrative calculations below, noting, however, once again that the sensor can consist also of just one sufficiently large ferro- or ferrimagnetic nanoparticle. For example, a particle with the size  $103 \times 85 \times 85 \text{ nm}^3$  will have about the same  $\mu B \approx 4.36 k_B T_r$  as our rod with  $n = 7$ , and such nanoparticles are also customly found in living species. Some examples of  $U(\phi)$  for various magnetic energies and the corresponding  $p(\phi)$  are plotted in Fig. 2.

Consider first the  $B = 0$  case (full line), and notice, that when  $U(\phi)$  arrives at its maximum at  $\phi_{\max} \approx 103.3^\circ$ ,  $p(\phi_{\max}) \approx 0.269$ . For  $\phi \geq \phi_{\max}$ , a further increase of  $\phi$  introduces a negative stiffness instability and the rod rotates to a new metastable minimum at  $\phi_{\min,2} \approx 144.81^\circ$ , where the channel opening probability becomes  $p(\phi_{\min,2}) \approx 0.926$ . At the first metastable minimum,  $\phi_{\min,1} = \phi_0 = 30^\circ$ ,  $p(\phi_{\min,1}) \approx 10^{-8}$ . The corresponding energy differences between two metastable minima is  $\Delta U = U(\phi_{\min,2}) - U(\phi_{\min,1}) \approx 0.3639 = 3.639 k_B T_r$ , and the energy barriers are  $\Delta U_1 = U(\phi_{\max}) - U(\phi_{\min,1}) \approx 0.787 = 7.87 k_B T_r$ , and  $\Delta U_2 = U(\phi_{\max}) - U(\phi_{\min,2}) \approx 0.4232 = 4.232 k_B T_r$ . Being attached to a common sensor the channels will fluctuate stochastically but synchronously between their closed and open states following the sensor motion, with the averaged opening probability which can be roughly estimated as  $\langle p \rangle \sim 1/[1 + \exp(\Delta U/(k_B T_r))] \approx 0.026$  (at room temperatures),

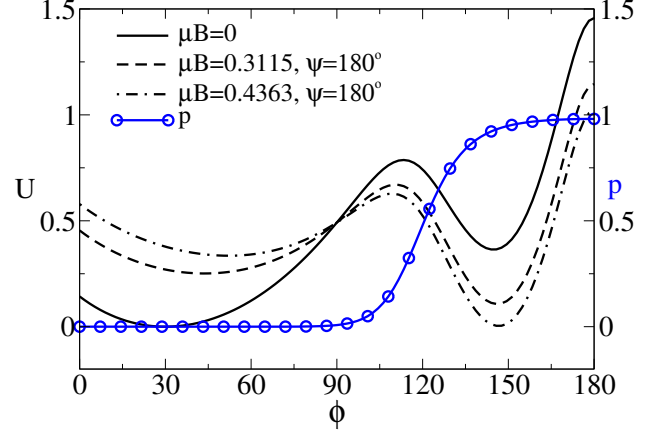


FIG. 2. (color online) Orientational potential  $U(\phi)$  and opening probability  $p(\phi)$  (blue line with circles) of ion channel versus angle  $\phi$  in degrees. Potential box walls are imposed for  $\phi < 0$  and  $\phi > \pi$  restricting motion to one side of membrane. Magnetic field is applied at the angle  $\psi = 180^\circ$ , and  $\phi_0 = 30^\circ$ . The model parameters:  $T = 0.1$ ,  $l_{\max} = 1.5$ ,  $f_0 = 1.5$ ,  $l_0 = 1.22$ , and  $m = 7$  channels in the sensor cluster. The gating energy difference  $\epsilon_2 - \epsilon_1 = f_0 l_0 = 1.83$ , or  $18.3$  in units of  $k_B T_r$ .

i.e. the channels are closed most of time. Actually, the opening probability will be lower than this rough estimate because the first minimum is shallower than the second one, i.e. it is also entropically preferred. Judging from the value of  $\Delta U$ , one can expect that for a sufficiently strong magnetic field at a proper angle  $\psi$  such that  $\mu B \sim \Delta U$ , the second metastable minimum can be made lower relative to the first one and the channel will become open on average. Indeed, this is the case already for  $\mu B = 0.3115 U_0 = 3.115 k_B T_r$  at  $\psi = \pi$ , see Fig. 2. The entropic effects may, however, compensate somewhat for the field-induced negative  $\Delta U$ , and the channels are indeed about half-open on average, see below. For a larger  $\mu B = 0.4363 U_0 = 4.363 k_B T_r$  in Fig. 2, the channels will predominantly be open.

#### A. Averaged open probability and ionic current as function of field direction

The averaged probability of the channel to be open can be found as

$$\langle p(B, \psi) \rangle = \int_0^\pi p(\phi) e^{-U(\phi)/(k_B T)} d\phi / Z, \quad (3)$$

where  $Z = \int_0^\pi e^{-U(\phi)/(k_B T)} d\phi$  is the corresponding statistical sum (integral). It accounts also for entropic effects. Unfortunately, this expression cannot be found in a closed compact analytic form for the model considered. However, its numerical evaluation can be easily done.

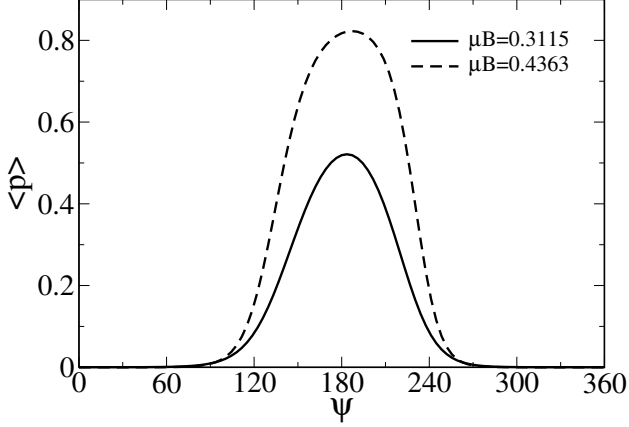


FIG. 3. Averaged probability of the channels to be open as function of magnetic field orientation for two values of  $\mu B$  shown in the plot. The model parameters:  $\phi_0 = 30^\circ$ ,  $T = 0.1$ ,  $l_{\max} = 1.5$ ,  $f_0 = 1.5$ ,  $l_0 = 1.22$ , and  $m = 7$  channels in the sensor cluster.

The corresponding results are shown in Fig. 3 and reveal that the direction of magnetic field can be detected by a bell-shaped increase of the opening probability within the angle  $\Delta\psi \sim 180^\circ \pm 60^\circ$ . Further sharpening of the detection of the field direction can be achieved via an adjusted threshold of excitation in the sensory cell.

The averaged ionic current conducted by this sensory complex is thus  $\langle I \rangle = m i_0 \langle p(B, \psi) \rangle$ , where  $i_0$  is unitary current through one open channel. Let us estimate it as  $i_0 = 50$  pA being a typical value for large conductance channels [33]. These should be either sodium, or calcium channels in order to cause depolarization of the cell membrane by their opening, given typically small out-of-equilibrium innercell concentrations of sodium and calcium ions with respect to the cell exterior. Then, for  $m = 7$  and  $\langle p \rangle = 0.5$ ,  $\langle I \rangle = 175$  pA. Estimating the whole cell membrane resistance at rest as  $R = 100$  M $\Omega$  [88], the transmembrane potential change is estimated as  $\Delta V = R \langle I \rangle \sim 17.5$  mV. This can already be sufficient to depolarize an excitable cell membrane and to trigger a spiking activity mediating further information about external magnetic field changes. However, a detailed elaboration of related excitable cell model in the spirit of the Hodgkin-Huxley type conductances based approach is beyond the scope of the present work and is left for a future.

### B. Stochastic dynamics

In order to operate as sensor, the opening-closing stochastic dynamics of the considered magnetic sensor should also be sufficiently fast. Clearly, if it would take minutes on average to accomplish transitions to the open

state, such a sensor would simply be too slow to be of any relevance in biology. The motion of sensor occurs in viscoelastic cytosol. It is considered to be overdamped with the inertial effects neglected. Apart from the mean torque  $f(\phi) = -dU(\phi)/d\phi$ , it is subjected to viscoelastic memory-friction torque  $-\int_0^t \eta_{\text{mem}}(t-t')\dot{\phi}(t')dt'$ , which acts in addition to the viscous Stokes friction torque,  $-\eta_0\dot{\phi}$ , caused by the primary water component of cytosol. The dissipative forces are complemented by the corresponding zero-mean Gaussian thermal random noises of the environment at temperature  $T$ ,  $\xi_{\text{mem}}(t)$  and  $\xi_0(t)$ , correspondingly. The friction and thermal noise are related by the (second) fluctuation-dissipation theorem (FDT) by Kubo [89–91]

$$\langle \xi_{\text{mem}}(t) \xi_{\text{mem}}(t') \rangle = k_B T \eta_{\text{mem}}(|t - t'|), \quad (4)$$

$$\langle \xi_0(t) \xi_0(t') \rangle = 2k_B T \eta_0 \delta(t - t'). \quad (5)$$

This ensures thermal detailed balance in the absence of external driving. Stochastic dynamics is described by the Generalized Langevin Equation (GLE) [89–92]

$$\eta_0 \dot{\phi} = f(\phi) - \int_0^t \eta_{\text{mem}}(t-t')\dot{\phi}(t')dt' + \xi_{\text{mem}}(t) + \xi_0(t). \quad (6)$$

The memory kernel reflecting viscoelasticity of complex polymeric fluids such as cytosol has often intermediate power law scaling  $\eta_{\text{mem}}(t) = \eta_\alpha t^{-\alpha}/\Gamma(1-\alpha)$ , between two memory cutoffs,  $\tau_l$  and  $\tau_h$ , with  $0 < \alpha < 1$ . It corresponds to a complex shear modulus  $G^*(\omega) \propto \omega^\alpha$  [50, 54], at intermediate frequencies in accordance with a huge body of rheology [93, 94] and microrheology research [51–54, 56, 57].  $\eta_\alpha$  is a fractional friction coefficient [48, 95] corresponding to a fractional viscosity coefficient  $\zeta_\alpha$  [93],  $\eta_\alpha \propto \zeta_\alpha$ . A strict power law is clearly an idealization and cutoffs must be present on physical grounds. The short time cutoff  $\tau_l$  reflects molecular size effects or highest vibrational modes present in the environment (which cannot be captured by any continuous medium type approximation). The long time cutoff  $\tau_h$  must also be present in any fluid-like environment making the overall integral  $\eta_{\text{eff}} = \int_0^\infty \eta_{\text{mem}}(t)dt$  finite. This reflects a finite macroscopic viscosity  $\zeta_{\text{eff}} \sim \eta_{\text{eff}}$  of such complex fluids on a large time scale  $t \gg \tau_h$ . The model with  $\tau_l \rightarrow 0$ ,  $\tau_h \rightarrow \infty$  (strict power law scaling) corresponds to the so-called fractional Langevin equation (FLE) upon using the formalism of fractional time derivatives [63, 69, 92, 96, 97], or a strict sub-Ohmic memory friction within dynamical approach to generalized Brownian motion [90, 98]. Then, the solution of a potential-free FLE (6),  $f(\phi) = 0$ , with the Stokes friction neglected,  $\eta_0 \rightarrow 0$ , and for  $\phi$  regarded as a linear, rather than cyclic variable, is fractional Brownian motion (fBm) [48, 63]. It presents a Gaussian process with stationary increments and a long-range memory, which is completely characterized by its variance,  $\langle \delta\phi^2 \rangle = 2D_\alpha t^\alpha/\Gamma(1+\alpha)$ , growing sublinearly. The fractional (orientational) diffusion coefficient  $D_\alpha$  is

related to fractional friction coefficient  $\eta_\alpha$  by the generalized Einstein relation,  $D_\alpha = k_B T / \eta_\alpha$ . Upon taking the Stokes friction into account it becomes [69],

$$\langle \delta \phi^2(t) \rangle = 2D_0 t E_{1-\alpha,2}[-(t/\tau_{in})^{1-\alpha}], \quad (7)$$

where  $E_{a,b}(z) := \sum_0^\infty z^n / \Gamma(an+b)$  is generalized Mittag-Leffler function, and  $D_0 = k_B T / \eta_0$  is a normal diffusion coefficient. Furthermore,  $\tau_{in} = (\eta_0 / \eta_\alpha)^{1/(1-\alpha)}$  is a transient time constant. For  $t \ll \tau_{in}$ , diffusion is initially normal,  $\langle \delta \phi^2(t) \rangle \approx 2D_0 t$ . It becomes anomalously slow,  $\langle (\delta \phi)^2 \rangle = 2D_\alpha t^\alpha / \Gamma(1+\alpha)$ , for  $t \gg \tau_{in}$ . We take further the advantage of approximation of the power-law scaling memory kernel by a sum of exponentials [47, 48]

$$\eta_{\text{mem}}(t) = \sum_{i=1}^N k_i \exp(-\nu_i t), \quad (8)$$

with a fractal scaling of relaxation rates  $\nu_i = \nu_0 / b^{i-1}$  and weights  $k_i \propto \nu_i^\alpha$  (having physical dimension of energy in the present case) to embed non-Markovian dynamics of  $\phi(t)$  as a component or projection of  $N+1$ -dimensional Markovian dynamics

$$\begin{aligned} \eta_0 \dot{\phi} &= f(\phi) - \sum_{i=1}^N k_i (\phi - y_i) + \xi_0(t), \\ \eta_i \dot{y}_i &= k_i (\phi - y_i) + \xi_i(t), \end{aligned} \quad (9)$$

where  $y_i$  are nondimensional linear auxiliary variables,  $\eta_i = k_i / \nu_i$ , and  $\xi_i(t)$  are independent auxiliary white Gaussian noises obeying

$$\langle \xi_i(t) \xi_j(t') \rangle = 2\delta_{ij} k_B T \eta_j \delta(t - t'), \quad (10)$$

and also independent of  $\xi_0(t)$ . The initial positions  $y_i(0)$  are sampled from a Gaussian distribution centered around  $\phi(0)$ ,  $\langle y_i(0) \rangle = \phi(0)$  with variances  $\langle [y_i(0) - \phi(0)]^2 \rangle = k_B T / k_i$ , in order to have complete equivalence with the corresponding GLE in Eqs. (4)-(6), (8) in the ensemble sense [48]. It is convenient to choose

$$k_i = \nu_0 \eta_{\text{eff}} \frac{b^{1-\alpha} - 1}{b^{(i-1)\alpha} [b^{N(1-\alpha)} - 1]}, \quad (11)$$

where  $\nu_0 = 1/\tau_l$  is the largest relaxation rate of environment equal to the inverse small time cutoff,  $\tau_l \ll \tau_{in}$ . Diffusion becomes again normal on the time scale  $t \gg \tau_h = \tau_l b^{N-1}$ , and  $\eta_\alpha = \eta_{\text{eff}} \tau_h^{\alpha-1} / g_\alpha$ , with a proportionality coefficient  $g_\alpha$  about unity,  $g_\alpha \sim 1$  [71]. For example,  $g_\alpha \approx 0.93$ , for  $\alpha = 0.4$  and  $N \geq 5$  [72]. The scaling coefficient  $b$  controls the quality of approximation of the power law dependence between two time cutoffs. Relative error is about 4% only already for a crude decade scaling with  $b = 10$ , which suffices in most studies, and improves further to 0.01% for  $b = 2$  [68]. Interestingly,  $\tau_h / \tau_{in} = (\eta_{\text{eff}} / \eta_0)^{1/(1-\alpha)}$  independently of  $b$ , which allows to estimate the time duration of intermediate subdiffusion in units of  $\tau_{in}$  from merely the knowledge of  $\alpha$  and an effective enhancement of friction in cytosol relative one in water in the long-time normal diffusion limit.

For example, if  $\tau_{in} \sim 1$  msec and  $\tilde{\eta}_{\text{eff}} = \eta_{\text{eff}} / \eta_0 = 10^3$  for  $\alpha = 0.5$ , intermediate subdiffusion will last until  $\tau_h \sim 10^3$  sec, i.e. it extends over six time decades in units of  $\tau_{in}$ . Such a consideration can be very useful to estimate  $\tilde{\eta}_{\text{eff}}$  from experimental data. We scale time in the units of  $\tau_{sc} = \eta_0 / U_0$ . For  $U_0 = 10 k_B T_r$  and for the rod of length  $L = 275$  nm consisting of 5 magnetosomes it is estimated as  $\tau_{sc} \approx 0.404$  msec, and for the rod of length 385 nm consisting of 7 magnetosomes  $\tau_{sc} \approx 0.905$  msec (see Appendix B). This corresponds to the rotational diffusion coefficients  $D_0 = 0.248$  rad<sup>2</sup>/msec, and  $D_0 = 0.110$  rad<sup>2</sup>/msec, respectively.

### C. Relaxation within a potential well

Nonlinear viscoelastic dynamics in a bistable potential is rather intricate [47]. To understand its main features, it is important to realize first the character of relaxation process in one potential well. This can be done within a parabolic well approximation,  $U(\phi) \approx \kappa_{1,2}(\phi - \phi_{\min,1,2})^2/2$ , where  $\kappa_{1,2} = d^2 U(\phi) / d\phi^2|_{\phi=\phi_{\min,1,2}}$ . The relaxation of an initial fluctuation,  $\delta\phi(0) = \phi(0) - \phi_{\min,1,2}$ , within a parabolic potential follows the relaxation law  $\langle \delta\phi(t) \rangle = \delta\phi(0)\theta(t)$ , with relaxation function  $\theta(t)$  whose Laplace-transform reads [48, 99]

$$\tilde{\theta}(s) = \frac{\tilde{\eta}(s)}{\kappa + s\tilde{\eta}(s)} \quad (12)$$

for arbitrary memory kernel  $\eta(t)$ . Here we omitted subindex 1,2 at  $\kappa$  for simplicity. The relaxation function coincides with the normalized *stationary* autocorrelation function of fluctuations or ACF,  $\langle \delta\phi(t_0) \delta\phi(t_0 + t) \rangle_{eq} / \langle \delta\phi^2 \rangle_{eq}$ , with  $\langle \delta\phi^2 \rangle_{eq} = k_B T / \kappa$ , which does not depend on time shift  $t_0$ . In other words, the Onsager regression property holds generically within this model, as shown in [99]. However, ACF depends generally on both time arguments and displays aging phenomenon [48, 99, 100]. In the present case,  $\tilde{\eta}(s) = \eta_0 + \eta_\alpha s^{\alpha-1}$ , and

$$\tilde{\theta}(s) = \frac{\tau_0 + \tau_r (s\tau_r)^{\alpha-1}}{s\tau_0 + 1 + (s\tau_r)^\alpha} = \frac{r + r_{1-\alpha} s^{\alpha-1}}{s + r + r_{1-\alpha} s^\alpha}, \quad (13)$$

where we denote  $\tau_0 = \eta_0 / \kappa$ ,  $\tau_r = (\eta_\alpha / \kappa)^{1/\alpha}$ , and  $r = 1/\tau_0$ ,  $r_{1-\alpha} = \eta_\alpha / \eta_0 = \tau_{in}^{\alpha-1}$ . Upon change  $\alpha \rightarrow 1-\alpha$ , i.e. identifying our present  $\alpha$  with  $1-\alpha$  in [101] and identifying our present  $\tau_0$  with  $\langle \tau \rangle$  therein one can see that this result coincides (up to a normalization factor) with one obtained in Ref. [101] for the stationary ACF of fluctuations in a very different model based on CTRW approach to relaxation phenomena. This another approach is featured by two parallel relaxation channels characterized by normal rate  $r$ , and fractional rate  $r_{1-\alpha}$ , correspondingly, and by a *finite* mean residence time  $\langle \tau \rangle = 1/r$ , see in [75, 101] for basic formulations and details. In [101], the corresponding spectral power of fluctuations,  $S(\omega)$ , and the response function  $\chi(\omega)$  are also presented and

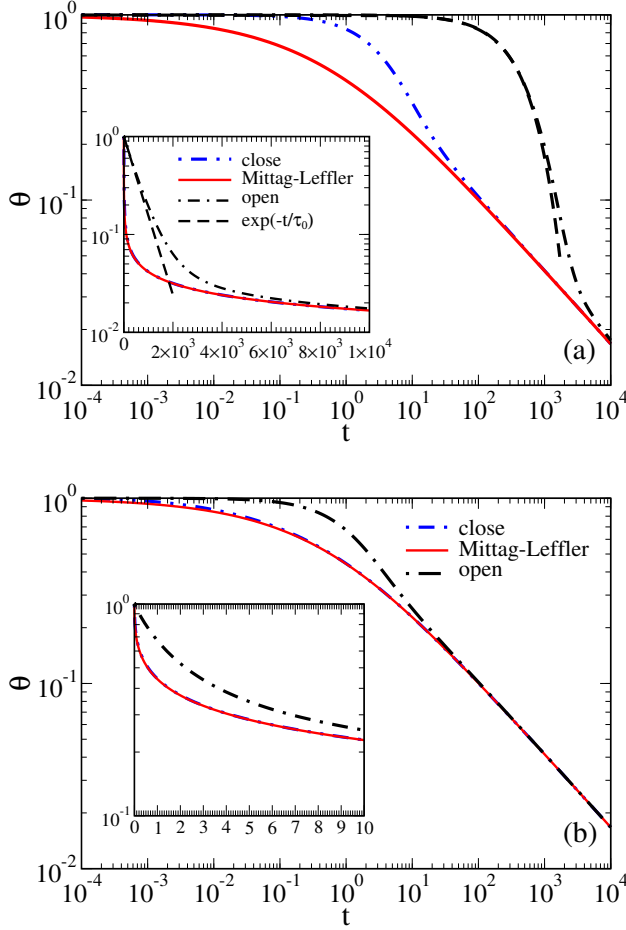


FIG. 4. (color online) Non-Markovian relaxation function against time in units of  $\tau_r$  for two different potential wells corresponding to a potential  $U(\phi)$  realization in Fig. 2 at  $\mu B = 0.3115$  for  $\alpha = 0.4$  in parabolic approximation and in neglect of the memory cutoff effects. Time constant  $\tau_r$  has different absolute values (in units of  $\tau_{sc} = \eta_0/U_0$ ) for different potential wells. Parts (a) and (b) correspond to two different values of fractional friction coefficient  $\eta_\alpha \sim \eta_{\text{eff}} \tau_h^{\alpha-1}$ . In (a),  $\tau_h = 10^4$  and  $\eta_{\text{eff}} = 100\eta_0$ ,  $z_1 = \tau_0/\tau_r = 4.838$  (for the relaxation in the first potential well which corresponds to closed times, see dash-double-dotted blue curve), and  $z_2 = \tau_0/\tau_r = 536.83$  (for the relaxation in the second potential well which corresponds to open times, dash-dotted black curve). Dashed black line depicts single-exponential approximation. Full red curve is the Mittag-Leffler relaxation function  $E_\alpha[-(t/\tau_r)^\alpha]$ , which corresponds to the Cole-Cole dielectric response and  $\beta$ -relaxation in glass-like materials. The tail of relaxation is universally a power law,  $\theta(t) \sim t^{-\alpha}$ . Inset in (a) shows the same plot on semi-logarithmic scale. It reveals that nearly 70% of initial relaxation in the second well occurs in the exponential regime. In (b),  $\eta_{\text{eff}}$  is increased to  $\eta_{\text{eff}} = 1000$ , with other parameters kept the same, which corresponds to a tenfold larger  $\eta_\alpha$ , as compare with the part (a). Here,  $z_1 = 0.01593$  (dash-double-dotted blue curve, which is difficult to see because it almost coincides with the full red line corresponding to the Mittag-Leffler relaxation), and  $z_2 = 1.6976$  (dash-dotted black curve). The relaxation in the first potential well is excellently described by the Mittag-Leffler relaxation function, and the relaxation in the second potential well is also clearly non-exponential all the time, as inset shows. Numerical results are obtained by numerical inversion of the Laplace-transform in Eq. (13) with Stehfest-Gaver method as described in Refs. [102, 103].

discussed. The relaxation behavior of  $\theta(t)$  depends very strongly on the relationship between  $\tau_0$  and  $\tau_r$ . The time constant  $\tau_r$  can be expressed through  $\tau_0$  and the above  $\tau_{in}$ , as

$$\tau_r = \tau_0 \left( \frac{\tau_0}{\tau_{in}} \right)^{1/\alpha}. \quad (14)$$

A salient feature is that  $\tau_r$  depends on the potential curvature  $\kappa$  only through  $\tau_0$ , and  $\tau_{in}$  that characterizes free diffusion. The Laplace-transform of relaxation function can be inverted exactly to the time domain for a special case  $\alpha = 0.5$ . Then, it reads

$$\begin{aligned} \theta(t) = & \frac{1}{2} \left( 1 + \frac{1}{\sqrt{1-4z}} \right) e^{(1-\sqrt{1-4z})^2 t / (4z^2 \tau_r)} \\ & \times \text{erfc} \left[ (1 - \sqrt{1-4z}) \sqrt{t / (4z^2 \tau_r)} \right] \\ & + \frac{1}{2} \left( 1 - \frac{1}{\sqrt{1-4z}} \right) e^{(1+\sqrt{1-4z})^2 t / (4z^2 \tau_r)} \\ & \times \text{erfc} \left[ (1 + \sqrt{1-4z}) \sqrt{t / (4z^2 \tau_r)} \right], \quad (15) \end{aligned}$$

where  $z = \tau_0/\tau_r$ , and  $\text{erfc}$  is complementary error function. Furthermore, for any  $0 < \alpha < 1$ , if  $\tau_0 \ll \tau_r$ , then relaxation follows approximately  $\theta(t) \approx E_\alpha[-(t/\tau_r)^\alpha]$ , see numerical results in Fig. 4 (b), for  $\alpha = 0.4$  and the relaxation in the first potential well (closed times), within the parabolic approximation. It is initially stretched exponential for  $t \ll \tau_r$ , and then a power law,  $\theta(t) \propto t^{-\alpha}$ . The spectral power of intrawell fluctuations is  $S(\omega) \propto 1/\omega^{1-\alpha}$ , at low frequencies, and such an intrawell motion is featured by the Cole-Cole response to external fields [99]. It is measured in many biological tissues [8], and corresponds to the so-called  $\beta$ -relaxation in glassy systems. Clearly, for a sufficient small  $\kappa$  and  $\tau_{in}$  such a regime can always be realized. Another regime with  $\tau_0 \gg \tau_r$  can also be very important. For a given  $\tau_{in}$ , it can always be realized for a sufficiently large  $\kappa$ , i.e. sufficiently stiff trapping potential. Then, the relaxation of  $\theta(t)$  starts universally from an exponential regime,  $\theta(t) = \exp(-t/\tau_0)$ , which changes into a power law tail  $\theta(t) \propto 1/t^\alpha$ , see in Fig. 4 (a), for  $\alpha = 0.4$  (open times), and also in Figs. 2 and 3 in [101] for  $\alpha = 0.5$ . The larger the ratio  $\tau_0/\tau_r$ , the smaller is the weight of a heavy tail. In other words, the major part of  $\theta(t)$  relaxation occurs exponentially for  $z \gg 1$ . The power law tail starts then from some  $\theta_c \ll 1$ . For example, in Fig. 4 (a), about 70% of the whole relaxation in the second potential well (open times) occurs in the exponential regime. The power law tail of open times has just a few percent weight therein, as the main double-logarithmic plot in Fig. 4 (a) reveals. And nevertheless it can be very important yielding to the  $S(\omega) \propto 1/\omega^{1+\alpha}$  feature of the fluctuations power spectrum for  $\tau_0^{-1} \ll \omega \ll \tau_r^{-1}$ . It has been detected e.g. experimentally in Ref. [60] for transversal fluctuations of cargo moving along a microtubule. Moreover, slow residual relaxation in the potential wells leads generally to a breakdown of the rate theory and validates the phys-



ical picture of slowly (on a characteristic time scale of transitions) fluctuating barriers and fluctuating rates.

#### D. Thermally activated transitions between metastable states of sensor

Despite transitions between the potentials wells cannot be described as a rate process for the biophysically most important case of intermediate barriers (less than about  $10 k_B T$  depending on  $\alpha$ ), in the case of power law memory kernels, the rate theory has been shown to be able to predict, at least in some cases, the most probable logarithm of residence times in the potential wells [47]. Moreover, the rate description is restored in the limit of very high barriers. Then, the transition rates  $R_{1,2}$  follow as

$$R_{1,2}(\mu) = \frac{\omega_{1,2}}{2\pi} \Xi(\mu) \exp(-\beta \Delta U_{1,2}), \quad (16)$$

where  $\omega_{1,2} = \sqrt{\kappa_{1,2}/J}$  are circular attempt frequencies, and  $0 \leq \Xi(\mu) \leq 1$  is the so-called transmission coefficient, which for the considered intermediate-to-strong friction limit is found [79, 83] as  $\Xi(\mu) = \mu/\omega_b$ . Here,  $\omega_b = \sqrt{\kappa_b/J}$  is the imaginary barrier frequency,  $\kappa_b = -d^2 U(\phi)/d\phi^2|_{\phi=\phi_{\max}}$ , and  $\mu$  is the renormalized barrier frequency. The latter one is found at the largest positive root of a transcendental equation taking (in the considered overdamped limit,  $J \rightarrow 0$ ) the general form  $\mu \tilde{\eta}(\mu) = \kappa_b$ , and for the memory kernel considered,  $\mu \eta_0 + \eta_\alpha \mu^\alpha = \kappa_b$ . By introducing  $\tau_0^{(b)} = \eta_0/\kappa_b$ , and  $\tau_r^{(b)} = (\eta_\alpha/\kappa_b)^{1/\alpha}$ , we can write it as

$$\tau_0^{(b)} \mu + (\tau_r^{(b)} \mu)^\alpha = 1. \quad (17)$$

For the memory kernel expanded into a sum of exponentials it takes on the form

$$\mu \left( \eta_0 + \sum_{i=1}^N \frac{k_i}{\mu + \nu_i} \right) = \kappa_b, \quad (18)$$

which can be rewritten as an algebraic equation of  $N+1$  degree for the unknown  $\mu$ . For a special case  $\alpha = 0.5$ , Eq. (17) can be solved exactly to yield  $\mu = 4[\tau_r^{(b)}]^{-1} / \left[ 1 + \sqrt{1 + 4\tau_0^{(b)}/\tau_r^{(b)}} \right]^2$ , and

$$R_{1,2} = \frac{1}{2\pi} \sqrt{\frac{\kappa_{1,2}}{\kappa_b}} \frac{1}{\tau_r^{(b)}} \frac{4 \exp(-\beta \Delta U_{1,2})}{\left[ 1 + \sqrt{1 + 4\tau_0^{(b)}/\tau_r^{(b)}} \right]^2}. \quad (19)$$

This insightful result can be expressed in terms of the normal diffusion ( $\eta_\alpha \rightarrow 0$ ) overdamped Kramers rate

$$\begin{aligned} R_{1,2}^{(0)} &= \frac{1}{2\pi} \sqrt{\frac{\kappa_{1,2}}{\kappa_b}} \frac{1}{\tau_0^{(b)}} \exp(-\beta \Delta U_{1,2}) \\ &= \frac{1}{2\pi} \frac{1}{\tau_0^{(b)}} \exp(-\beta \Delta G_{1,2}) \end{aligned} \quad (20)$$

as

$$R_{1,2} = R_{1,2}^{(0)} F(z_b = \tau_0^{(b)}/\tau_r^{(b)}), \quad (21)$$

where

$$F(z) = \frac{4z}{[1 + \sqrt{1 + 4z}]^2}. \quad (22)$$

Notice that in the second line of Eq. (20), we incorporated the difference of the curvatures  $\kappa_1$  and  $\kappa_2$  as *additional* entropic contributions to the free energy barriers,  $\Delta G_{1,2} = \Delta U_{1,2} - T \Delta S_{1,2}^{(ad)}$  with entropy differences  $\Delta S_{1,2}^{(ad)} = k_B \ln(\kappa_{1,2}/\kappa_b)/2$ . Generally, reduction of a multidimensional dynamics to a two-state dynamics contains such important additional entropic contributions. It should be mentioned, however, that in our model  $U(\phi)$  in Eq. (2) is also temperature-dependent, i.e. is in fact (Gibbs) free energy profile. We consider, however, a fixed value of temperature throughout the paper. The correct separation of  $\Delta G_{1,2}$  into the internal energy (or rather enthalpic) part  $\Delta H_{1,2}$ , and entropic part  $-T \Delta S_{1,2}$  must always be done using fundamental thermodynamic relation  $\Delta H = \Delta G + T \Delta S = \Delta G - T(\partial \Delta G / \partial T)_P$  [104].

Furthermore, for  $z \ll 1$  in (22),  $F(z) \approx z$ , and for  $z \gg 1$ ,  $F(z)$  approaches unity,  $F(z) \rightarrow 1$ . Hence, in the parameter regime  $\tau_0^{(b)} \gg \tau_r^{(b)}$ , which correlates with  $\tau_0 \gg \tau_r$ , see above,  $R_{1,2} \approx R_{1,2}^{(0)}$ , i.e. the rate is practically not affected by subdiffusion. This is a very important result, which is valid also for other values of  $\alpha$ . It is very different from the suppression by the factor  $\eta_{\text{eff}}/\eta_0$ , which some unjustified intuition might suggest. This result shows that subdiffusion does not necessary suppress the activation rates, in accordance with our earlier results in [47] obtained in the presence of inertial effects. Here, the inertial effects were, however, entirely neglected. Moreover, it will be shown elsewhere that in the presence of inertial effects the transmission factor for subdiffusive dynamics can arrive at its maximal value of unity, in the case of cusp-like potential barriers  $\kappa_b \gg \kappa_{1,2}$ . The combination of nonlinearity and viscoelastic subdiffusion is really counterintuitive and paradoxical! An essential suppression of rate occurs in the regime  $\tau_0^{(b)} \ll \tau_r^{(b)}$ , which correlates with  $\tau_0 \ll \tau_r$ , i.e. when the Mittag-Leffler relaxation within potential wells covers most of time. Then, we obtain (for arbitrary  $\alpha$ )

$$R_{1,2} \approx \frac{1}{2\pi} \sqrt{\frac{\kappa_{1,2}}{\kappa_b}} \frac{1}{\tau_r^{(b)}} \exp(-\beta \Delta U_{1,2}). \quad (23)$$

Notice that it is smaller than  $R_{1,2}^{(0)}$  by the factor  $\tau_0^{(b)}/\tau_r^{(b)}$ .

### III. RESULTS

#### A. Markovian dynamics

We performed first stochastic simulations of Markovian memoryless dynamics ( $\eta_\alpha \rightarrow 0$ ) for the same parameters



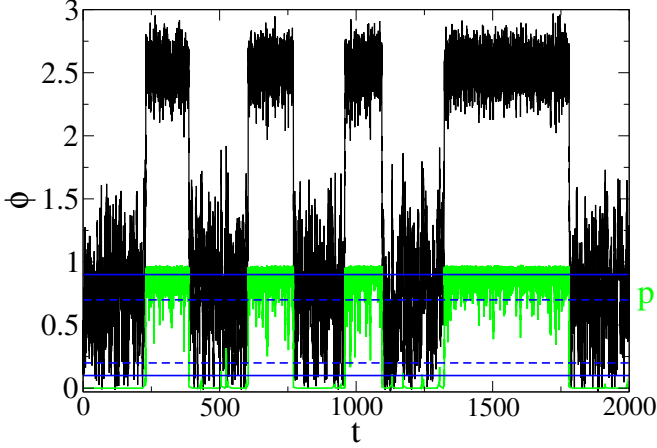


FIG. 5. (color online) Trajectory realization of Markovian memoryless dynamics. Black line describes stochastic rotational fluctuations of sensor, while the green (light gray) line depicts fluctuations of the probability of the gate to be open (and normalized ion current fluctuations). The blue horizontal lines depict some detection thresholds (two possible sets are shown). The model parameters:  $T = 0.1$ ,  $\mu B = 0.3115$ ,  $\phi_0 = \pi/6$ ,  $\psi = \pi$ ,  $l_{\max} = 1.5$ ,  $f_0 = 1.5$ ,  $l_0 = 1.22$ , and  $m = 7$  channels in the sensor cluster.

as in Figs. 2, 3,  $\psi = \pi$ , with time step  $\delta t = 2 \cdot 10^{-6}$  using stochastic Heun method, in accordance with our previous studies. A typical trajectory of bistable fluctuations for  $\mu B \approx 3.12 k_B T_r$  is shown in Fig. 5. One can see characteristic bistable fluctuations of sensor orientation. It flips between two metastable positions (interwell fluctuations) and exhibits also profound fluctuations within potential wells (intrawell fluctuations). The open-shut dynamics reveals a new flickering feature, apart from large amplitude fluctuations reflecting bistability of sensor. Flickering comes about from intrawell fluctuations of sensor corresponding to its open metastable state, see below.

The statistics of transitions can be determined from one very long single trajectory by setting different detection thresholds, e.g.  $p_1 = 0.2$  and  $p_2 = 0.7$  (set 1), or  $p_1 = 0.1$  and  $p_2 = 0.9$  (set 2). One can also relate thresholds to the minima of  $U(\phi)$  (set 3). For example, for  $\mu B = 0.3115$  in Fig. 2,  $\phi_{\min,1} \approx 0.762 \approx 43.69^\circ$ ,  $\phi_{\min,2} \approx 2.551 \approx 146.13^\circ$ , and for  $\mu B = 0.4363$  in Fig. 2,  $\phi_{\min,1} \approx 0.910 \approx 52.14^\circ$ ,  $\phi_{\min,2} \approx 2.559 \approx 146.63^\circ$ . With this choice,  $\phi_{\min,1}$  corresponds to a very small  $p_1 \sim 10^{-8} - 10^{-6}$ , and  $\phi_{\min,2}$  to  $p_2 \sim 0.92 - 0.95$ . Yet, an experimentalist can prefer the choice  $p_1 = 0.5$  and some  $p_2 > p_1$ , e.g.  $p_2 = 0.9$  (set 4). It must be emphasized that the statistics of transitions can very essentially depend on the thresholds, i.e. on how the current signal is detected. This is because there are very fast events even within the purely Markovian version of the considered dynamics, where very short outbursts occur from the open state to the closed state, when the probability

of the channel to be open becomes briefly less than one-half. The lower the low detection threshold  $0 < p_1 \leq 0.5$  in Fig. 5, the larger is the number of missed short closure events. This is why the averaged residence times in the states do increase with lowering  $p_1$ , when the bursting events are increasingly disregarded. The explanation of a highly bursting character of dynamics even in the absence of memory effects can easily be grasped from Fig. 2. Indeed the maximum of the potential  $U(\phi)$  corresponds to the opening probability  $p \sim 0.17 - 0.27$ , depending on  $\mu B$  value in Fig. 2. Hence, an essential part of closure dynamics occurs when the sensor moves within the second metastable minimum of sensor not reaching the transition state of sensor. This observation is also quite generally of a great importance within the context of gating dynamics of other ionic channels. It emphasizes the importance of a very complex molecular structure of ionic channels [105], where the sensory part and the gating part are generally not the same and their mechanical coupling can be very important in all fine details. Our treatment makes this implicit complexity quite obvious within a simplest model setting. The opening probability of the channel defined as a time average,  $p = \langle \tau_o \rangle / (\langle \tau_o \rangle + \langle \tau_c \rangle)$ , is, however, weakly sensitive to the choice of the detection thresholds, and agrees reasonably well with the ensemble averaged result depicted in Fig. 3, where  $p \approx 0.52$  at  $\mu B = 0.3115$  and  $\psi = \pi$ .

Transitions from open to closed state are regarded as accomplished by a downward crossing of the low threshold. In turn, transitions from closed to open state are accomplished by an upward crossing of the high threshold. In this way, one finds pairs of random time intervals in the closed,  $\tau_c$ , and open,  $\tau_o$ , states whose statistics is subsequently studied. For a very long trajectory of the kind depicted in Fig. 5, the survival probabilities  $P_o(\tau)$  and  $P_c(\tau)$ , which correspond to residence time distributions,  $\psi_i(\tau) = -dP_i(\tau)/\tau$ ,  $i = o, c$ , are shown in Fig. 6, (a)-(d). They are derived from the same single very long trajectory by using different sets of thresholds. As a test of ergodicity (in distribution), we derived probability density  $\hat{P}(\phi)$  of sensor orientations from a single trajectory and compared it with the ensemble equilibrium  $P_{\text{eq}}(\phi) \propto \exp[-U(\phi)/(k_B T)]$ . Excellent agreement (not presented) implies ergodicity. In Fig. 6, we provide fits of the tail of distributions with the exponential functions  $c_i \exp(-\tau/\tau_i)$ , weight  $c_i$  and time constant  $\tau_i$ . Furthermore, the initial part of closed time distribution therein is nicely fitted by the 4-th type Pareto law with survival probability [106]

$$P(\tau) = \frac{1}{[1 + (\tau/\tau_p)^{\gamma_1}]^{\gamma_2}}. \quad (24)$$

For  $\tau \gg \tau_p$ ,  $P(\tau) \propto \tau^{-\gamma}$  with  $\gamma = \gamma_1 \gamma_2$ . It reflects the short time bursting dynamics. Notice that in Fig. 6 (a) the open time distribution is almost single exponential,  $c_o \approx 0.966$ , while the weight of the exponential tail of closed time distribution is about  $c_c \approx 0.4$  only, and nearly 60% of distribution is described by the Pareto law

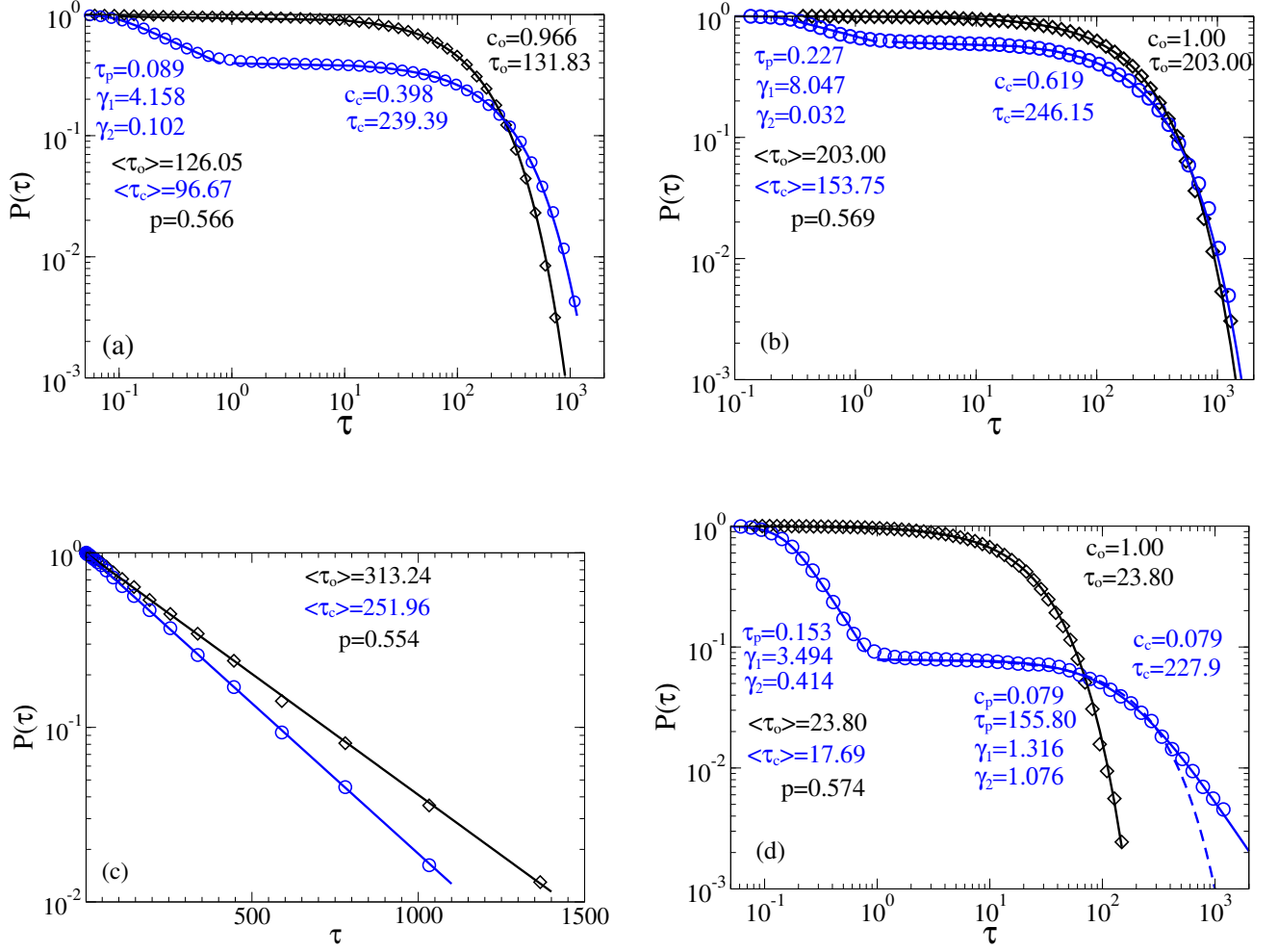


FIG. 6. (color online) Survival probabilities of open (black diamond symbols), and closed (blue open circles) times derived from numerical data for the case  $\mu B = 0.3115$ ,  $\psi = \pi$ ,  $\phi_0 = \pi/6$ , using different sets of detection thresholds: (a)  $p_1 = 0.2$ ,  $p_2 = 0.7$ ; (b)  $p_1 = 0.1$ ,  $p_2 = 0.9$ , (c) for the minima of  $U(\phi)$  used as detection thresholds,  $p_1 = p(\phi_{\min,1})$ ,  $p_2 = p(\phi_{\min,2})$ ; (d)  $p_1 = 0.5$ ,  $p_2 = 0.9$ . Lines present the corresponding exponential,  $c_i \exp(-\tau/\tau_i)$ , or Pareto law (24) fits with the parameters shown in the plots. The mean residence times, as well as the opening probability  $p = \langle\tau_o\rangle/(\langle\tau_o\rangle + \langle\tau_c\rangle)$  are also shown. Notice a strong dependence of these fits on the detection thresholds used. Other parameters:  $T = 0.1$ ,  $l_{\max} = 1.5$ ,  $f_0 = 1.5$ ,  $r_0 = 1.22$ , and  $m = 7$  channels in the sensor cluster.

(24). With lowering the detection threshold  $p_1$  in Fig. 6 (b) to  $p_1 = 0.1$  the weight of exponential tail increases to  $c_c \approx 0.62$ . This is because less bursting events are detected. The variation of the time constant  $\tau_c$  describing mean residence time in the closed state with a variation of detection thresholds in Fig. 6 (a)-(c) is not statistically significant. Notice, that a two-stage relaxation of the closed times  $P(\tau)$  cannot be described by a simple sequential Markovian scheme with just two closed sub-states,  $C_2 \leftrightarrow C_1 \rightarrow O$ . This is because: (i) the relative weight of two stages depends very essentially on the detection threshold, (ii) initial stage is described by the Pareto power law (24) and not by an exponential.

Furthermore, if to detect transitions by crossing  $p_{1,2}$

levels corresponding to the minima of  $U(\phi)$  (set 3) then the survival probabilities become practically single exponential, see in Fig. 6 (c), where the mean times coincide with the corresponding time constants. In this case, the bursts within long opening events are completely neglected. The mean residence times increase accordingly. The standard Kramers rate result in (20) gives  $R_1^{(0)} \approx 0.0038052$  and  $R_2^{(0)} \approx 0.0030899$ . The corresponding inverse values  $1/R_1^{(0)} \approx 262.80$  and  $1/R_2^{(0)} \approx 323.63$  agree with  $\langle\tau_c\rangle \approx 251.96$  and  $\langle\tau_o\rangle \approx 313.24$ , correspondingly, in Fig. 6 (c) within a 4% error margin. This is a typical accuracy of our stochastic simulations. However, if to use  $p_1 = 0.5$  for the lower threshold, what experimentalists can prefer, and to keep  $p_2 = 0.9$ , a more

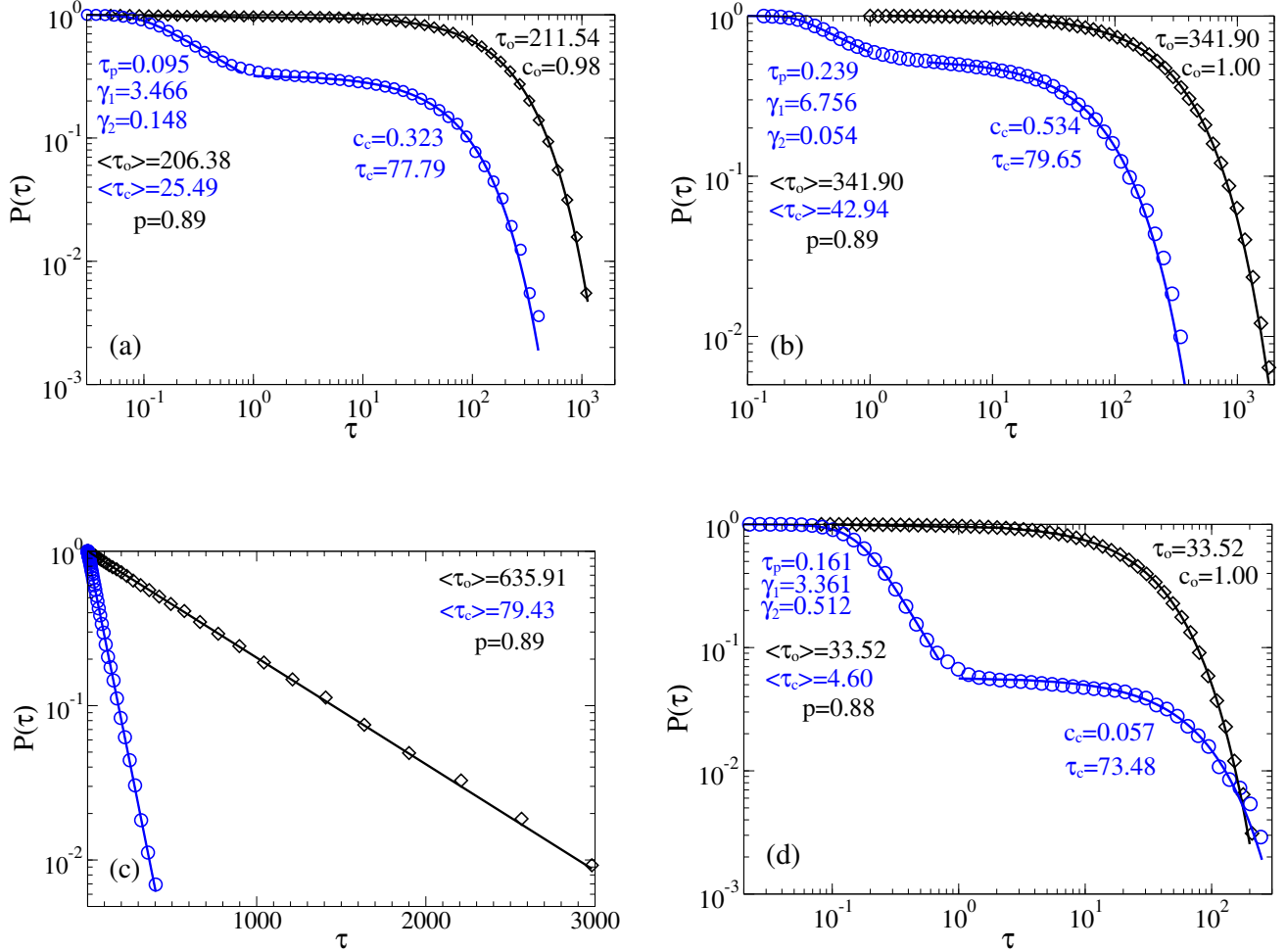


FIG. 7. (color online) Survival probabilities of open (black diamond symbols), and closed (blue open circles) times derived from numerical data for the case  $\mu B = 0.4363$ ,  $\psi = \pi$  using different sets of detection thresholds: (a)  $p_1 = 0.2$ ,  $p_2 = 0.7$ ; (b)  $p_1 = 0.1$ ,  $p_2 = 0.9$ , (c) for the minima of  $U(\phi)$  used as detection thresholds,  $p_1 = p(\phi_{\min,1})$ ,  $p_2 = p(\phi_{\min,2})$ ; (d)  $p_1 = 0.5$ ,  $p_2 = 0.9$ . Lines present the corresponding exponential,  $c_i \exp(-\tau/\tau_i)$ , and the Pareto law (24) fits with the parameters shown in the plots. The mean residence times, as well as the opening probability  $p = \langle \tau_o \rangle / (\langle \tau_o \rangle + \langle \tau_c \rangle)$  are also displayed. Notice a strong dependence of these fits on the detection thresholds used. Other parameters:  $T = 0.1$ ,  $l_{\max} = 1.5$ ,  $f_0 = 1.5$ ,  $r_0 = 1.22$ , and  $m = 7$  channels in the sensor cluster.

complex picture emerges for the closed residence times, see in Fig. 6 (d). It reveals two characteristic power law regimes described by Pareto laws. The initial Pareto law describes almost 90% of the probability decay with  $\gamma = \gamma_1 \gamma_2 = 1.405$ . It corresponds to the residence time distribution  $\psi(\tau) \propto \tau^{-\delta}$ , with  $\delta = 1 + \gamma = 2.405$ . Interestingly, similar power laws were indeed derived from experimental recordings of large conductance BK ion channels [40], which resemble the open-shut dynamics in our Fig. 5. However, a very different phenomenological theory has been proposed earlier for such a gating dynamics [46]. The second Pareto law part (24) in Fig. 6 (d) has weight  $c_p \approx 0.079$  and describes thus about last 8% of decay. Unexpectedly, an exponential tail fit of the data for the closed times in Fig. 6 (d) is worse, although

its time constant correlates with one in Fig. 6 (c), as expected. The distribution of open times remains, however, practically single exponential independently of thresholds with a threshold-dependent time constant. Our results show that a continuous-state Markovian bistable dynamics can explain such experimental non-Markovian features (within a contracted two-state non-Markovian dynamics), as bursting and power law distributions of the residence times. They can be caused by a nontrivial interplay of coupled sensor and gate dynamics, as well as threshold levels used for detection. What we measure depends really on how we detect. This is a signature of complex dynamics. Notice that the opening probability within the two-state interpretation of continuous state dynamics is rather robust with respect to the choice of

the detection thresholds. It agrees fairly with the ensemble average in (3) done for the continuous-state dynamics.

With increasing the number of magnetosomes in the sensor rod to  $n = 7$  (or for a correspondingly larger single nanoparticle used as sensor), the probability of channels to be open in the magnetic field of the Earth increases to over  $p = 0.8$  at a proper field orientation, see in Fig. 3. The residence times statistics displays similar features, see in Fig. 7 (a)-(d). Namely, the open times are nearly exponentially distributed, whereas the distribution of closed times depends strongly on the lower detection threshold. The lower the threshold, the closer is distribution to a single exponential. The rate theory yields  $R_1^{(0)} \approx 0.012306$ , and the corresponding  $1/R_1^{(0)} \approx 81.26$  agrees well, within 2.25 % error margin, with the numerical value of mean close time  $\langle \tau_c \rangle \approx 79.43$  in Fig. 7 (c). For the corresponding open times, the rate theory yields  $1/R_2^{(0)} \approx 708.11$ , which agrees in this case somewhat worse, within 10.2% error margin with numerical  $\langle \tau_o \rangle \approx 635.91$  in Fig. 7 (c). However, experimentalists can reveal power law features related to bursting, if they set  $p_1 = 0.5$ , or somewhat lower. So, in Fig. 7 (d) Pareto law with  $\gamma = \gamma_1 \gamma_2 \approx 1.721$  covers about 94% of the survival probability decay of the closed time distribution, which ends by an exponential tail with the weight of about 5.7% and decay time constant  $\tau_c$  which weakly depends on the choice of threshold, see in Fig. 7, from (a) to (d). The Pareto law describes durations of closed time intervals within a burst, whereas the time constant  $\tau_c$  corresponds approximately to the mean time interval between the bursts, when the channels are well closed. Clearly, the time constant of open times  $\tau_o$  depends very essentially on the choice of lower detection threshold.

Our results show that if the sensor motion would occur in water its dynamics would be reasonably fast being in hundreds of milliseconds range. Hence, it could serve as a detector for quasi-static or slowly changing magnetic fields. However, in cytosol the effective friction  $\eta_{\text{eff}}$  is enhanced dramatically for the particles of a typical size of magnetosomes. Kirschvink *et al.* estimated  $\tilde{\eta}_{\text{eff}} = \eta_{\text{eff}}/\eta_0$  by a factor of  $\tilde{\eta}_{\text{eff}} = 100$  [12, 21]. If to just renormalize the Stokes friction by this factor, the effective time scale  $\tau_{sc}$  would enlarge accordingly,  $\tau_{sc} \rightarrow (\tilde{\eta}_{\text{eff}} + 1)\tau_{sc}$ . Then, our sensor would be really too slow to be functional. However, accounting for non-Markovian memory effects by a naive renormalization of the friction coefficient is patently wrong within the context of thermally activated dynamics, as it is well-recognized within non-Markovian generalizations of Kramers rate theory [79–83]. Therefore, it is compelling to clarify the role of low-dimensional non-Markovian memory effects.

### B. Role of memory effects

Stochastic simulations of Eq. (9) were done for the following additional parameters,  $\alpha = 0.4$  [59, 60, 72, 73],  $\nu_0 = 10^4$ ,  $N = 9$  and  $b = 10$ . Hence,  $\tau_l = 10^{-4}$

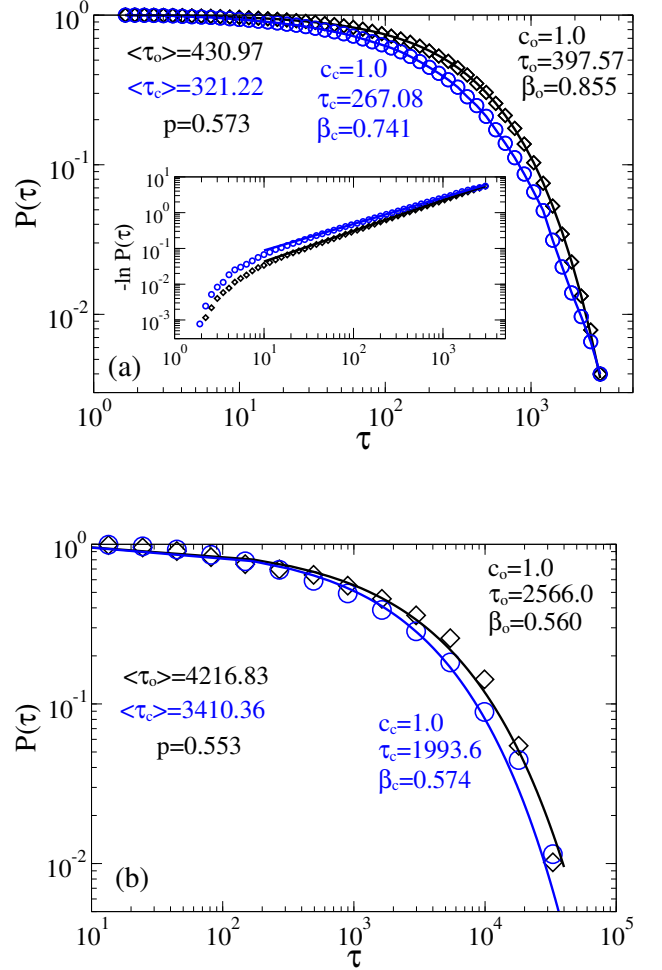


FIG. 8. (color online) Survival probabilities of open (black diamond symbols), and closed (blue open circles) times derived from numerical data for the case  $\mu B = 0.3115$ ,  $\psi = \pi$ , using the detection thresholds defined by the minima of  $U(\phi)$ ,  $p_1 = p(\phi_{\min,1})$ ,  $p_2 = p(\phi_{\min,2})$ , for (a)  $\eta_{\text{eff}} = 100$ , and (b)  $\eta_{\text{eff}} = 1000$ . Lines present the corresponding stretched exponential,  $c_i \exp[-(\tau/\tau_i)^{\beta_i}]$ , fits with the parameters shown in the plots. The mean residence times, as well as the opening probability  $p = \langle \tau_o \rangle / (\langle \tau_o \rangle + \langle \tau_c \rangle)$  are also displayed. Other parameters:  $T = 0.1$ ,  $l_{\max} = 1.5$ ,  $f_0 = 1.5$ ,  $l_0 = 1.22$ , and  $m = 7$  channels in the sensor cluster.

and  $\tau_h = 10^4$ . The latter time is about 4.04 sec for  $\tau_{sc} \approx 0.404$  msec, or about 9.05 sec for  $\tau_{sc} \approx 0.905$  msec. Furthermore, we used two values of  $\eta_{\text{eff}}$ ,  $\eta_{\text{eff}} = 100$ , and  $\eta_{\text{eff}} = 1000$ , which correspond to two different values of  $\eta_\alpha = \eta_{\text{eff}} \tau_h^{\alpha-1} / g_\alpha$  in simulations, and the rotational subdiffusion coefficients  $D_\alpha \approx 0.360 \text{ rad}^2/\text{msec}^{0.4}$  and  $D_\alpha \approx 0.036 \text{ rad}^2/\text{msec}^{0.4}$  at  $\tau_{sc} \approx 0.404$  msec, or  $D_\alpha \approx 0.260 \text{ rad}^2/\text{msec}^{0.4}$  and  $D_\alpha \approx 0.026 \text{ rad}^2/\text{msec}^{0.4}$  at  $\tau_{sc} \approx 0.905$  msec, respectively. In this respect, one can enlarge both  $\eta_{\text{eff}}$  and  $\tau_h$  (by using a larger  $N$ ), while keeping  $\eta_\alpha$  the same. For example, by taking  $N = 11$ , and

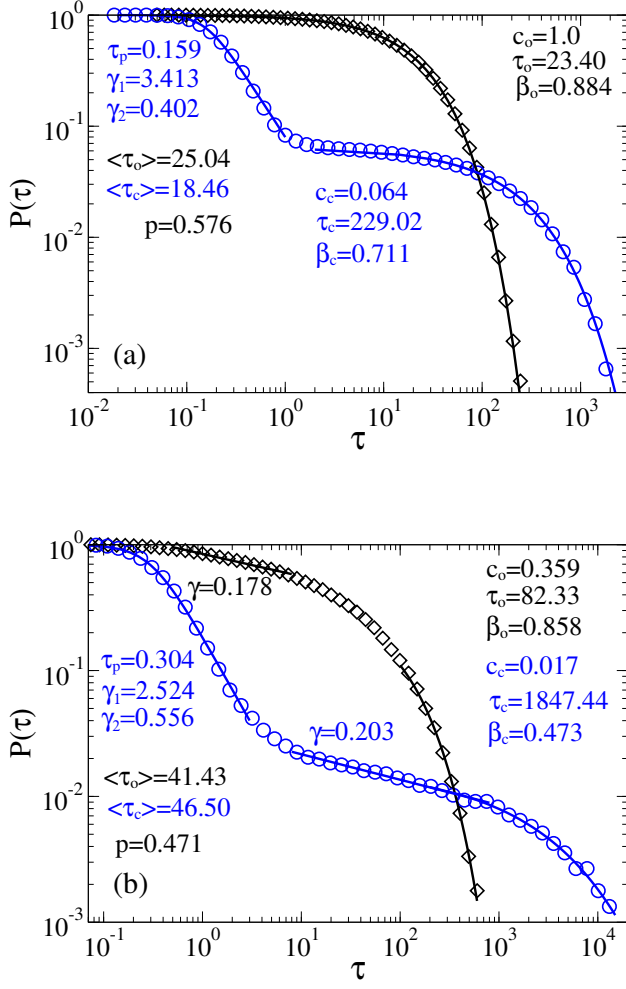


FIG. 9. (color online) Survival probabilities of open (black diamond symbols), and closed (blue open circles) times derived from numerical data for the case  $\mu B = 0.3115$ ,  $\psi = \pi$ , using the detection thresholds  $p_1 = 0.5$  and  $p_2 = 0.9$  for (a)  $\eta_{\text{eff}} = 100$ , and (b)  $\eta_{\text{eff}} = 1000$ . Lines present the corresponding stretched exponential,  $c_i \exp[-(\tau/\tau_i)^{\beta_i}]$ , Pareto law (24), and power law,  $\sim \tau^{-\gamma}$ , fits with the parameters shown in the plots. The mean residence times, as well as the opening probability  $p = \langle \tau_o \rangle / (\langle \tau_o \rangle + \langle \tau_c \rangle)$  are also displayed. Other parameters:  $T = 0.1$ ,  $l_{\text{max}} = 1.5$ ,  $f_0 = 1.5$ ,  $l_0 = 1.22$ , and  $m = 7$  channels in the sensor cluster.

enlarging  $\tau_h$  to about 404 sec and 905 sec, correspondingly, we can keep  $\eta_\alpha$  the same by enlarging  $\eta_{\text{eff}}$  from 100 to approximately 1585 and from 1000 to approximately 15850, respectively. Furthermore, for the used parameters we have  $\tau_{in} \approx 4.64$  for  $\eta_{\text{eff}} = 100$ , and  $\tau_{in} \approx 0.01$  for  $\eta_{\text{eff}} = 1000$ . For  $\tau_{sc} \approx 0.404$  msec, this corresponds to  $\tau_{in} \approx 1.88$  msec ( $\eta_{\text{eff}} = 100$ ) or  $\tau_{in} \approx 0.04$  msec ( $\eta_{\text{eff}} = 1000$ ). Furthermore, for  $\tau_{sc} \approx 0.905$  msec, this corresponds to  $\tau_{in} \approx 4.20$  msec ( $\eta_{\text{eff}} = 100$ ) or  $\tau_{in} \approx 0.09$  msec ( $\eta_{\text{eff}} = 1000$ ).

The first striking universal feature of the influence

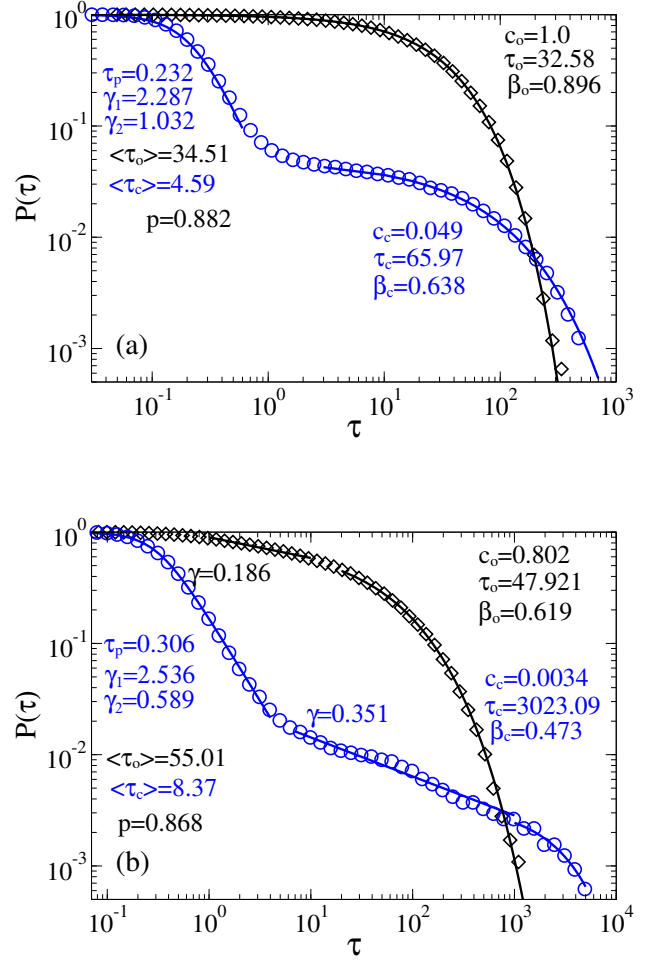


FIG. 10. (color online) Survival probabilities of open (black diamond symbols), and closed (blue open circles) times derived from numerical data for the case  $\mu B = 0.4346$ ,  $\psi = \pi$ , using the detection thresholds  $p_1 = 0.5$  and  $p_2 = 0.9$  for (a)  $\eta_{\text{eff}} = 100$ , and (b)  $\eta_{\text{eff}} = 1000$ . Lines present the corresponding stretched exponential,  $c_i \exp[-(\tau/\tau_i)^{\beta_i}]$ , Pareto law (24), and power law,  $\sim \tau^{-\gamma}$ , fits with the parameters shown in the plots. The mean residence times, as well as the opening probability  $p = \langle \tau_o \rangle / (\langle \tau_o \rangle + \langle \tau_c \rangle)$  are also displayed. Other parameters:  $T = 0.1$ ,  $l_{\text{max}} = 1.5$ ,  $f_0 = 1.5$ ,  $l_0 = 1.22$ , and  $m = 7$  channels in the sensor cluster.

of viscoelastic memory effects is the emergence of a stretched exponential distribution  $c_i \exp[-(\tau/\tau_i)^{\beta_i}]$ ,  $0 < \beta_i < 1$  out of formerly exponential one, compare Fig. 6 (c) and Fig. 8 (a), where  $\eta_{\text{eff}} = 100$ , for other parameters being the same in both figures, and detection thresholds set at the minima of  $U(\phi)$ . In Fig. 8 (a), the residence time distributions (RTDs) become stretched exponential (Weibull distribution) to a good degree,  $c_o \approx 1$ ,  $c_c \approx 1$ , except for some initial times, see in the inset, where a deviation from linear dependence of  $-\ln P(\tau) \propto (\tau/\tau_i)^{\beta_i}$  plotted on the double-



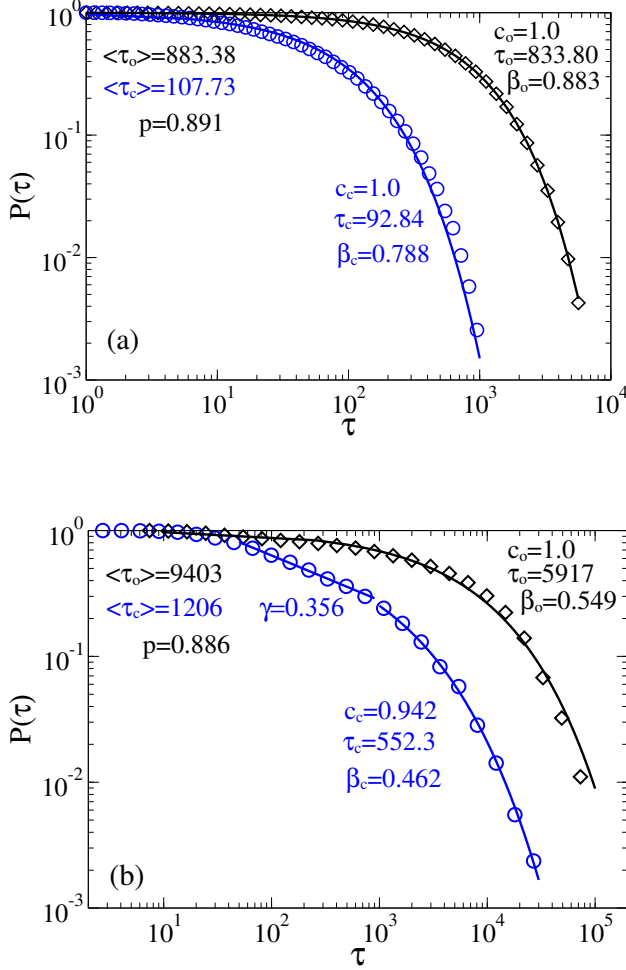


FIG. 11. (color online) Survival probabilities of open (black diamond symbols), and closed (blue open circles) times derived from numerical data for the case  $\mu B = 0.4363$ ,  $\psi = \pi$ , using the detection thresholds defined by the minima of  $U(\phi)$ ,  $p_1 = p(\phi_{\min,1})$ ,  $p_2 = p(\phi_{\min,2})$ , for (a)  $\eta_{\text{eff}} = 100$ , and (b)  $\eta_{\text{eff}} = 1000$ . Lines present the corresponding stretched exponential,  $c_i \exp[-(\tau/\tau_i)^{\beta_i}]$ , and power law fits with the parameters shown in the plots. The mean residence times are also shown along with the opening probability  $p = \langle \tau_o \rangle / (\langle \tau_o \rangle + \langle \tau_c \rangle)$ . Other parameters:  $T = 0.1$ ,  $l_{\max} = 1.5$ ,  $f_0 = 1.5$ ,  $l_0 = 1.22$ , and  $m = 7$  channels in the sensor cluster.

logarithmic scale becomes seen. For this choice of thresholds, we can compare the results of non-Markovian rate theory (NMRT), namely the Grote-Hynes result in Eqs. (16), (17) with our numerics for the particular memory kernel studied. As observed in Ref. [47], the Grote-Hynes result is capable to describe the most probable value of the logarithmically transformed residence times,  $\ln \tau$ , even beyond the strict rate regime, when RTDs become profoundly non-exponential. For the case of Weibull distribution characterized by the survival probability  $P_i(\tau) = \exp[-(\tau/\tau_i)^{\beta_i}]$ , and non-Markovian rate

$R(\tau) = -d \ln P(\tau)/d\tau = \beta_i \tau_i^{-1} / (\tau/\tau_i)^{1-\beta_i}$ , the correspondingly transformed distribution of  $y = \ln \tau$  has its maximum at  $y_{\max} = \ln \tau_i$ . Hence, in accordance with [47] NMRT is expected to yield  $\tau_i$  of Weibull distribution as  $\tau_i = R_i^{-1}$ . For the results depicted in Fig. 8 (a), the Grote-Hynes result yields  $R_i = 0.8169 R_i^{(0)}$ , for the exact memory kernel, where  $R_i^{(0)}$  is the overdamped Kramers result. It has been already discussed above in relation to our numerical results presented in Fig. 6 (c). Hence, NMRT yields  $\tau_{o,\text{exact}}^{(\text{NMRT})} \approx 396.17$  and  $\tau_{c,\text{exact}}^{(\text{NMRT})} \approx 321.70$ , for the exact memory kernels. For the memory kernels approximated by a sum of exponentials, we obtain  $\tau_o^{(\text{NMRT})} \approx 395.30$ ,  $\tau_c^{(\text{NMRT})} \approx 321.00$ . Notice that the kernel approximation introduces an error of about 0.2% only in theoretical NMRT results! The value  $\tau_{o,\text{exact}}^{(\text{NMRT})} \approx 396.17$  agrees very well with  $\tau_o = 397.57$  in Fig. 8 (a). The difference is less than 0.4%! Furthermore,  $\tau_{c,\text{exact}}^{(\text{NMRT})} \approx 321.70$  somewhat overestimates numerical  $\tau_c \approx 267.08$ . However, it agrees well with the numerical average  $\langle \tau_c \rangle \approx 321.22$ . Also for the results in Fig. 8 (b), where we increase  $\eta_{\text{eff}}$  to  $\eta_{\text{eff}} = 1000$ , for the same other parameters, NMRT yields  $\tau_{o,\text{exact}}^{(\text{NMRT})} \approx 2531.56$  and  $\tau_{c,\text{exact}}^{(\text{NMRT})} \approx 2055.68$ , for the exact memory kernels, and  $\tau_o^{(\text{NMRT})} \approx 2450.84$  and  $\tau_c^{(\text{NMRT})} \approx 1990.13$ , for the approximate kernels. The error due to the memory kernel approximation now increases to about 3.2%.  $\tau_{o,\text{exact}}^{(\text{NMRT})} \approx 2531.56$  agrees with  $\tau_o \approx 2566.0$  derived from the numerical data using maximum likelihood fitting within 1.4% error margin. Also  $\tau_{c,\text{exact}}^{(\text{NMRT})} \approx 2055.68$  agrees with the maximum likelihood value  $\tau_c \approx 1993.6$  within 3% error margin. Notice that deviation from the numerical mean values,  $\langle \tau_o \rangle \approx 4216.83$  and  $\langle \tau_c \rangle \approx 3410.36$  in this case is very essential. In this respect, NMRT describes the most probable  $\ln \tau$  generally much better than the mean residence time  $\langle \tau \rangle$ . Only in the strict rate regime or for  $\beta_i$  close to one does NMRT describe well  $\langle \tau \rangle$ , which coincides with the effective inverse rate thus defined, and is also the so-called stationary flux-over-population rate [83]. Our results confirm that NMRT is of a high predictive value even beyond the strict rate regime [47, 48]. What it, however, cannot do is to predict the form of non-exponential residence time distributions, or detailed course of non-Markovian kinetics.

Furthermore, in Fig. 9 the results are depicted for the same anomalous kinetics discussed in Fig. 8, but for the detection thresholds  $p_1 = 0.5$  and  $p_2 = 0.9$  (set 4). For the smaller value of  $\eta_\alpha$  in Fig. 9 (a), one can see, by comparison with Fig. 6 (d) that the initial Pareto law for the closed times is not changed dramatically. This is because on the corresponding initial time scale dynamics is nearly normal. The profound changes are reflected by the tail of the closed time survival probability and by the whole open time distribution, which are stretched exponential. The average residence times are only slightly enlarged. However, with the increase of  $\eta_\alpha$  some further changes

become detectable in Fig. 9 (b). Namely, the mean residence times increase, which is expected, however, not so strongly as for another detection threshold choice, compare with Fig. 8 (b). Next, an initial power law regime can be revealed in the distribution of open times, and the weight of a stretched exponential tail is only  $c_o \approx 0.359$  versus  $c_o \approx 1$  in Fig. 9 (a), where stretched exponential covers practically over all essential transition times (except for very short times, see inset in Fig. 8 (a)). Also an intermediate power law emerges for closed times in Fig. 9 (b), and the weight of stretched exponential tail becomes smaller:  $c_c \approx 0.017$  in Fig. 9 (b) vs.  $c_c \approx 0.064$  in Fig. 9 (a). Moreover, the initial Pareto law is also changed in Fig. 9 (b). This is because for larger  $\eta_{\text{eff}} = 1000$  diffusion is not normal anymore on the related time scale. Similar characteristic features hold also for other choices of thresholds, see in Supplement [107].

For the same detection thresholds, but a larger  $\mu B = 0.4163$  the results are depicted in Fig. 10 (a), (b). These results are to be compared with the results in Fig. 7 (d), in the absence of non-Markovian effects. Again, for a smaller  $\eta_\alpha$  ( $\eta_{\text{eff}} = 100$ ), the mean residence times are almost not influenced, albeit the initial power law parameters in the survival probability of closed times are somewhat changed. The most essential typical change is conversion of exponential residence time distribution of open times and an exponential tail of the closed time distribution into the stretched exponential dependencies. The larger  $\eta_\alpha$  in Fig. 10 (b) leads to expectedly larger mean residence times, and smaller  $\beta_i$  of stretched exponential tails. Notice also the emergence of an intermediate power law for the closed times, and an initial power law regime for the open times. Furthermore, survival probabilities corresponding to the thresholds set in accordance with the  $U(\phi)$  minima are shown in Fig. 11. They are clearly stretched exponential in Fig. 11 (a) with the parameters derived using the maximum likelihood criterion. In this case, NMRT predicts  $\tau_{o,\text{exact}}^{(\text{NMRT})} \approx 887.93$  and  $\tau_{c,\text{exact}}^{(\text{NMRT})} \approx 101.90$ , for the exact memory kernels, and  $\tau_o^{(\text{NMRT})} \approx 885.68$ ,  $\tau_c^{(\text{NMRT})} \approx 101.64$ , for the approximate ones.  $\tau_{o,\text{exact}}^{(\text{NMRT})}$  agrees with the numerical  $\tau_o \approx 833.8$  within 6.1% error margin, while the agreement of  $\tau_{c,\text{exact}}^{(\text{NMRT})}$  with the numerical  $\tau_c \approx 92.84$  is worse, about 8.9% discrepancy. Interestingly, in this case the mean values,  $\langle \tau_o \rangle \approx 883.38$  and  $\langle \tau_c \rangle \approx 107.73$  agree with the results of NMRT theory better, within 0.51% and 5.72% error margins for the exact memory kernels. This shows that for larger  $\beta_i$ , like  $\beta_o = 0.883$  and  $\beta_c = 0.788$  in this plot the difference between  $\tau_i$  determined from the most probable  $\ln \tau_i$  and the corresponding mean values  $\langle \tau_i \rangle$  can be within the actual statistical errors of our simulations. In Fig. 11 (b), the results for  $\eta_{\text{eff}} = 1000$  are presented, at the same other parameters. In this figure, a maximum likelihood fit by a stretched exponential with  $\beta_o \approx 0.549$  and  $\tau_o \approx 5.917 \times 10^3$  is shown for the open time distribution. The closed time kinetics is more complex. It reveals an intermediate power

law,  $\gamma \approx 0.356$ , and a stretched exponential tail, and therefore is not expected to be described by NMRT. Let us compare the analytical NMRT results with the numerical results depicted in Fig. 11 (b). NMRT yields  $\tau_{o,\text{exact}}^{(\text{NMRT})} \approx 6.817 \times 10^3$  and  $\tau_{c,\text{exact}}^{(\text{NMRT})} \approx 0.782 \times 10^3$ , for the exact memory kernels, and  $\tau_o^{(\text{NMRT})} \approx 6.553 \times 10^3$  and  $\tau_c^{(\text{NMRT})} \approx 0.752 \times 10^3$ , for the approximate memory kernels used in simulations. The error introduced by the memory kernel approximation is about 3.9% in this case. The numerical mean values obtained on 1267 transitions (which required about 9 weeks of simulations),  $\langle \tau_o \rangle \approx 9.403 \times 10^3$ , and  $\langle \tau_c \rangle \approx 1.207 \times 10^3$  are larger than  $\tau_{o,c}^{(\text{NMRT})}$  by 43.5% and 60.5%, correspondingly. At the same time, the maximum likelihood value  $\tau_o \approx 5.917 \times 10^3$  deviates from  $\tau_o^{(\text{NMRT})}$  by about 6.6% only. However, NMRT clearly fails to describe characteristic features of the closed time distribution, which has a significant power law part. Two-dimensional densities corresponding to Fig. 11 (a), and Fig. 11 (b) in Supplement [107], see Figs. 3 and 4 therein, respectively, provide some important additional insight in this respect.

#### IV. DISCUSSION

We generalized a gating spring model of ion channels open-shut dynamics originally proposed for ion channels in stereocilia of hair cells [34] in application to hypothetical ion channels involved in magnetosensing [12]. Our modeling displays several generic features beyond the particular model considered. This makes it pertinent to other ionic channels in living cells, where a generalized coordinate of gating variable and sensor can be very different. For example, sensor is presented by charged  $\alpha$ -helices in the case of voltage-sensitive ion channels [105]. First striking generic feature is that sensor moves typically in a viscoelastic environment, rather than a simple fluid-like medium. In the present model this is cytosol. However, it can be also biological membrane, or ion channel protein macromolecule itself, with a sensory part relocating inside the macromolecule. We showed that viscoelasticity alone can explain the physical origin of stretched exponential and power law distributions of open and shut residence times. As a matter of fact, they emerge already within a standard double-well description of the sensor energetics with well defined potential wells, rather than due to a flat or rugged free energy landscape (another possibility). The neglect of medium's viscoelasticity leads immediately to distinct single-exponential distributions of the sensor residence times within our model, see in Figs. 6 (c) and 7 (c). Hence, viscoelasticity can be the primary physical reason of complex non-exponential gating dynamics – the explanation, which has apparently been overlooked thus far. Second, we treat the gating spring elasticity within a nonlinear FENE model, where a maximal extension length of linker is taken into account. It is more phys-



ical than a standard harmonic spring model. Next, the probability  $p(\phi)$  of a channel to be open does not reflect one-to-one the characteristic features of the sensor potential  $U(\phi)$ . This is, in fact, a generic feature of the gating spring model, which is not related in principle to viscoelasticity or nonlinear elastic effects. However, this fundamental feature has also been overlooked earlier. In our model, the value  $p(\phi) = 0.5$  when the channel is half-open belongs to the attraction domain of sensor open state, rather than to the potential barrier (transient state) separating two domains of attraction, and the barrier value  $p_b = p(\phi_{\max})$  can be as small as  $p_b \sim 0.1$ , depending on  $\mu B$  and  $\psi$ . Even in the Markovian memoryless case, this leads to a profoundly bursting character of the ion current recordings reflecting  $p(\phi(t))$  fluctuations within the open state of sensor, see in Fig. 5. Theorists can believe that the most rigorous way to calculate the residence time distributions in open and closed states of channel is to use the detection thresholds placed at the minima of  $U(\phi)$ . For a purely Markovian dynamics such a procedure leads to single-exponential distributions of residence times of *sensor*, see Fig. 6 (c) and Fig. 7 (c), with the mean residence times given by the inverse of Kramers rate. However, experimentalists can proceed differently. After detecting a bursting character of *ion current* fluctuations, like in our Fig. 5, an experimentalist is expected to put one detection threshold at  $p_1 = 0.5$  and another one somewhere at  $p_2 > p_1$  [108], e.g. at  $p_2 = 0.9$ , as in our Fig. 6 (d) and Fig. 7 (d). Then, he or she would find a Pareto distribution (24) of closed residence times within a burst with power law exponents  $\gamma = \gamma_1\gamma_2 \approx 1.45$  in Fig. 6 (d), and  $\gamma = \gamma_1\gamma_2 \approx 1.72$  in Fig. 7 (d), within the main power law regimes. One expects that this power law will end in an exponential tail which corresponds to interburst distances associated with large-amplitude relocations of sensor between the minima of  $U(\phi)$ . Indeed, the tail is single exponential in Fig. 7 (d), with weight  $c_c \approx 0.057$  and  $\tau_c \approx 73.48$  which roughly corresponds to  $\langle\tau_c\rangle \approx 79.43$  in Fig. 7 (c). A corresponding single-exponential fit in Fig. 6 (d) is, however, not that good, and a Pareto law fit the same weight  $c_p = c_c \approx 0.079$  and  $\gamma = \gamma_1\gamma_2 \approx 1.42$  is visually better. This happened clearly by chance, in a very particular case. Indeed, by choosing different thresholds in Figs. Fig. 6 (a), (b) one can see that there generally exists an exponential tail with a time constant which roughly corresponds to  $\langle\tau_c\rangle$  in Fig. 6 (c). This latter one is nicely described by the inverse Kramers rate. The weight  $c_c$  depends strongly on the choice of thresholds. The open times are nearly exponentially distributed in all parts of Figs. 6, 7, with the time constants which depend strongly on the threshold choice. Important is that even if the mean residence times and the detailed structure of survival probabilities do strongly depend on the choice of thresholds, the time averaged portion of open time  $p = \langle\tau_o\rangle/(\langle\tau_c\rangle + \langle\tau_o\rangle)$  is not changed dramatically. Its value approximately corresponds to the ensemble average depicted in Fig. 3 at  $\psi = \pi$ . This implies not only ergodicity, but also that

a two-state reduction of continuous state dynamics is a reasonable one. With  $\tau_{sc} \approx 0.404$  msec and  $\tau_{sc} \approx 0.905$  msec estimated for the rods consisting of  $n = 5$  and  $n = 7$  magnetosomes, correspondingly (see in Appendix B) one has  $\langle\tau_c\rangle \approx 7.15$  msec and  $\langle\tau_o\rangle \approx 9.62$  msec in Fig. 6 (d), as well as  $\langle\tau_c\rangle \approx 4.16$  msec and  $\langle\tau_o\rangle \approx 30.34$  msec in Fig. 7 (d). These are typical time scales for ion channel gating dynamics. However, with the bursts neglected the characteristic times lie in the hundreds of milliseconds range, which defines a characteristic time scale of the reaction of such a detector on changes of external magnetic field.

Furthermore, even in the absence of memory effects our model can explain the origin of power law distributions of closed times,  $\psi_c(\tau) \propto \tau^{-\delta}$ , with  $\delta = 1 + \gamma$  in some range around  $\delta = 2.5$ , as our numerical results imply. Similar bursting fluctuations with  $\delta \approx 2.24$  and exponentially distributed open times were indeed found in the locust large conductance BK channels [40]. A proper generalization for BK channels is, however, out of the scope of this work. It is reserved for a future. In this respect, one should mention that a very different phenomenological model was suggested earlier to rationalize bistable dynamics of BK channels in terms of a fractional conformational dynamics [46].

Our sensor operates, however, in viscoelastic cytosol, and a common line of reasoning is to account for the enlarged effective cytosol viscosity by using  $\eta_{\text{eff}}$  instead of  $\eta_0$  within a Markovian Langevin dynamics [12]. This would mean the enlargement of  $\tau_{sc}$  and the corresponding  $\langle\tau_c\rangle$  and  $\langle\tau_o\rangle$  by about the same factor. Then, already for  $\eta_{\text{eff}} = 100\eta_0$  [12] the mean opening and closing times would become so large that such a magnetosensitive channel could not be of any potential relevance as biosensor. It would be far too slow. However, our results obtained by a proper treatment of non-Markovian memory effects show that such simplistic estimations can be very misleading. Our model channel can yet be functional in viscoelastic environment. It must be stressed that  $\eta_{\text{eff}}$  can only be finite, if subdiffusion is transient and normal diffusion is established again for  $t \gg \tau_h$ . The central role is played in fact by the fractional friction coefficient  $\eta_\alpha \sim \eta_{\text{eff}}\tau_h^{\alpha-1}$ , and not by  $\eta_{\text{eff}}$ . Given the same  $\eta_\alpha$ ,  $\eta_{\text{eff}} \sim \tau_h^{1-\alpha}$ . By comparison of the results in Fig. 9 (a) with the corresponding Markovian case depicted in Fig. 6 (d) one establishes that the mean open and closed times are changed a little, for  $\eta_{\text{eff}} = 100\eta_0$  and  $\tau_h = 4.04$  sec ( $n = 5$ ), or  $\tau_h = 9.05$  sec ( $n = 7$ ). Also the initial Pareto law regime for the closed times is almost not affected in Fig. 9 (a). This is because non-Markovian memory effects are still not at play on the relevant time scale smaller than  $\tau_{in}$  of free subdiffusion. Diffusion is normal on that time scale. The latter feature is, however, not universally valid, see below, because (i)  $\tau_{in} \sim \tau_h(\eta_0/\eta_{\text{eff}})^{1/(1-\alpha)}$  is strongly influenced by  $\eta_{\text{eff}}$  at fixed  $\tau_h$ , and (ii) the transition from initially normal dynamics to subdiffusional is also strongly affected by the presence of potential. Furthermore, the tails of distributions are changed dramatically. They became stretched

exponential, in agreement with [47, 48], as a major manifestation of viscoelastic effects. The stretched exponential tail of the closed time distribution describes the distribution of interburst time intervals, as it can be understood from Fig. 8 (a), where the bursts are neglected. The distribution of both open and closed times is almost stretched exponential in Fig. 8 (a), except for an initial stage (see inset in this figure). The mean residence times are somewhat enhanced with respect to Markovian case in Fig. 6 (a), in a good agreement with NMRT. The other choices of thresholds in Figs. 1 (a) and 2 (a) of Supplement [107] confirm these main features. Moreover, for a larger  $\mu B$  in Fig. 10 (a) one observes similar features by comparison with Fig. 7 (d): The mean residence times are about the same (within typical numerical error margins), and the exponential tails turn into the stretched exponential ones. However, the initial Pareto distribution in this cases is changed.

The observed features provide a general physical explanation for the emergence of stretched exponential distributions in the statistics of ion channel fluctuations, as observed first by Liebovitch *et al.* [35]. Our theory explains it as a manifestation of viscoelastic memory effects for the sensor dynamics in cytosol. This explanation is rather general. It is expected to hold also for other models of ion channel gating dynamics with sensor moving within the membrane, or within the membrane protein itself. One should stress that the discussed results for fixed values of  $\eta_{\text{eff}}$  and  $\tau_h$  are not expected to visibly change, if we enlarge  $\tau_h$  and  $\eta_{\text{eff}}$  so that  $\eta_\alpha$  is not changed. This is because the main features we discuss are observed for the time intervals less than  $\tau_h$  in our figures. A typical length of single stochastic trajectories used to obtain these figures exceeds greatly  $\tau_h$ , and the diffusion becomes again normal on that time scale. What does matter indeed is the anomaly of diffusion caused by the memory of viscoelastic medium on the relevant time scales of transitions. For example, if we enhance  $\tau_h$  by a factor of 100 (using two additional auxiliary Brownian particles in our simulations), and enhance  $\eta_{\text{eff}}$  by the factor of  $100^{1-\alpha} \approx 15.9$  (for the used  $\alpha = 0.4$ ),  $\eta_\alpha$  is not changed, and we do not expect any significant changes of the results discussed. However, if we increase  $\eta_{\text{eff}}$  by the factor of ten at the same  $\tau_h$ ,  $\eta_\alpha$  is tenfold increased, and this results into the further qualitative changes observed. What does matter indeed even for a finite  $\tau_h$  is the fractional friction coefficient  $\eta_\alpha$ .

Indeed, for  $\eta_{\text{eff}} = 1000$  with the same  $\tau_h$ , the qualitatively new additional features are observed in the part (b) of Figs. 9, 10, see also in Figs. 1 (b) and 2 (b) of Supplement [107]. First, an initial power law emerges in the open time distribution, and a novel intermediate power law emerges in the closed time distribution. The mean residence times are essentially increased for the case with detection thresholds placed at  $U(\phi)$  minima, see in Figs. 8 (b), 11 (b). However, in Figs. 9 (b) and 11 (b) they are a little increased (less than doubled). Hence, the gating dynamics of our model channel remains in a

physiologically acceptable range. Such a sensor would slowly operate, yet be suitable to detect quasi-static or slowly changing magnetic fields. We see also how intermediate power law distributions can emerge naturally due to viscoelastic memory effects. Clearly, our theoretical approach is not restricted by a particular model of magnetosensitive ion channels we proposed and studied in this work.

## V. CONCLUSIONS

In this paper we proposed and studied a novel model of magnetosensitive ion channels featured by a bistable magnetosensor moving in viscoelastic cytosol. It is shown that a cluster of ionic channels gated by such a sensor can operate for realistic parameters and provide a tentative explanation for biological manifestations of the influence of weak magnetic fields, in particular, such as navigation of different biological species in the magnetic field of Earth, as suggested earlier by Kirschvink *et al.* Our model provides also a natural explanation of the origin of stretched exponential and power law distributions in the statistics of ion current fluctuations as ones caused by the viscoelasticity of the medium in which the sensor operates. We believe that our study will spark a further interest, both theoretical and experimental to the hypothesis of magnetosensitive ion channels, and to physical modeling of anomalous dynamics of ion channels and other proteins in living cells.

## ACKNOWLEDGMENT

Support of this research by the Deutsche Forschungsgemeinschaft (German Research Foundation), Grant GO 2052/1-2 is gratefully acknowledged.

## Appendix A: Estimation of magnetic moments and magnetic field strengths

Consider a sphere of magnetite with radius  $R$  and saturation magnetization  $M_s = 4.8 \cdot 10^5$  A/m. Assuming that it is magnetically ordered allows to calculate its magnetic moment as  $\mu = (4/3)\pi R^3 M_s$ , which for a sphere of radius  $R = 100$  nm yields  $\mu \approx 2.01 \times 10^{-15}$  A · m<sup>2</sup>. The energy of such a sphere in the magnetic field of Earth estimated as  $B_e = 50$   $\mu$ T is  $E_M = \mu B_e \approx 10^{-19}$  J  $\approx 24.5$   $k_B T_r$  with  $k_B T_r = 4.1 \times 10^{-21}$  J = 4.1 pN · nm. The magnetic field produced by such a magnetic nanoparticle at the distances  $r = |\vec{r}| \geq R$  from its center is the same as one of the point magnetic dipole  $\mu$  located at its center [109],

$$\vec{B}(\vec{r}) = \frac{\mu_0}{4\pi} \left( \frac{3\vec{r}(\vec{\mu}\vec{r})}{r^5} - \frac{\vec{\mu}}{r^3} \right), \quad (\text{A1})$$

where  $\mu_0 = 4\pi \times 10^{-7}$  T · m/A is magnetic permittivity of vacuum. This field is highly anisotropic and its maximal

value near to the surface of particle is

$$B_{\max} = \frac{\mu_0}{2\pi} \frac{\mu}{R^3} = \frac{2}{3} \mu_0 M_s \approx 0.402 \text{ T}. \quad (\text{A2})$$

This is a very large field as compare with  $B_e$ ! Notice that it does not depend on the particle radius and scales as  $B_{\max}(R/r)^3$  with the distance  $r \geq R$  from its center. Hence, up to the distances of about  $r = 20 R$  the maximum of the field produced by such a magnetic nanoparticle is larger than external  $B_e$ . For  $R = 100 \text{ nm}$ , the corresponding distance is about  $2 \mu\text{m}$ , a typical size of the bacterial cell. Given large  $E_M$ , such a particle is easily reoriented in the magnetic field of Earth. Together with a large  $B_{\max}$  this provides a ground for the assertions that even quantum mechanisms can be mediated by endogenous magnetic field of a magnetosome, rather than directly caused by the external magnetic field of Earth. Also spatial gradient of such an endogenous magnetic field is large on nanoscale.

Furthermore, the magnetic energy of dipole-dipole interaction of two identical nanospheres separated by distance  $r \geq 2R$  is

$$E_{dd} = V_{dd}(\sin \varphi_1 \sin \varphi_2 - 2 \cos \varphi_1 \cos \varphi_2) \quad (\text{A3})$$

in the approximation of point dipoles. Here, one assumes for simplicity that the magnetic moments lie in a common plane making angles  $\varphi_1$  and  $\varphi_2$  with the line connecting their centers. Furthermore,

$$V_{dd} = 10^{-7} \frac{16}{9} \pi^2 M_s^2 R^3 \left( \frac{R}{r} \right)^3, \quad (\text{A4})$$

which for the spheres in the close contact,  $r = 2R$ , is

$$V_{dd} = 10^{-7} \frac{2}{9} \pi^2 M_s^2 R^3. \quad (\text{A5})$$

For  $R = 100 \text{ nm}$ , this yields  $V_{dd} \approx 5.05 \times 10^{-17} \text{ J} \approx 1.23 \times 10^4 k_B T_r$ . This is a huge energy! Even for  $R = 10 \text{ nm}$ ,  $V_{dd} \approx 12.3 k_B T_r$  is still large. This explains why such magnetic nanoparticles tend to make magnetically ordered chains at ambient temperatures, which are clearly seen in magnetotactic bacteria.

Several further remarks are required. First,  $R = 100 \text{ nm}$  is about the maximal size of a spherical particle made of magnetite which possesses a permanent magnetic moment at ambient temperatures [10, 11]. Larger spherical particles do not possess a permanent magnetic moment. They are in a multidomain superparamagnetic state. However, if the particle is elongated it can still be in a ferrimagnetic state at ambient temperatures. Next, the preferable direction of the magnetic moment is not

completely fixed by the magnetic anisotropy of  $\text{Fe}_3\text{O}_4$  crystal, and the form of particle. Thermally agitated it can flip its direction to the opposite one, i.e. small nanoparticles are in fact intrinsically bistable. The corresponding thermal magnetic reorientation time (Neel relaxation time) exponentially depends on the particle volume. So, for  $R = 11.5 \text{ nm}$  it is about  $0.1 \text{ s}$  only. However, already for  $R = 15 \text{ nm}$  it is as large as  $10^9 \text{ s}$  [92], p. 125, or about 32 years, i.e. a metastable state can be considered as physically stable from a practical point of view. Furthermore, physical anisotropy of nanoparticle, e.g. an elongated ellipsoidal form, or the form of a rectangular parallelepiped further stabilizes the single domain structure. Many biomagnetite particles have proper sizes to be in the ferrimagnetic state. Typical sizes considered in this paper ensure ferrimagnetic state at room and physiological temperatures. Notice also that the dipole-dipole interaction can also dramatically stabilize ferromagnetic order for small particles like  $R = 10 \text{ nm}$  assembled into a chain.

## Appendix B: Estimation of characteristic physical time scale of dynamics

Here, we estimate the rotational friction coefficient of a rod of length  $L$  and diameter  $d$  in fluid of viscosity  $\zeta_0$  following [110]. For this we use the rotational “end-over-end” diffusion coefficient  $D_0$  [110] and the Einstein relation  $\eta_0 = D_0/(k_B T)$ . As a result,

$$\eta_0 = \frac{\pi \zeta_0 L^3}{3 [\ln p + C]}, \quad (\text{B1})$$

where  $p = L/d$  is aspect ratio and

$$C = -0.662 + 0.917/p - 0.050/p^2, \quad (\text{B2})$$

which is valid for  $p = 2 - 20$ . For magnetosome of size  $a \times b \times b$  and the rod of length  $L = na$ , we approximate  $d \approx b$ , and  $p \approx na/b$ . Hence,

$$\eta_0 \approx n^3 \frac{\pi \zeta_0 a^3}{3 [\ln(na/b) + C]}, \quad (\text{B3})$$

and

$$\tau_{sc} \approx n^3 \frac{\zeta_0 a^3}{U_0} \frac{\pi}{3 [\ln(na/b) + C]}. \quad (\text{B4})$$

In water,  $\zeta_0 \sim 1 \text{ mPa} \cdot \text{sec}$  at  $T = 20^\circ\text{C}$ , and for  $U_0 = 41 \text{ pN} \cdot \text{nm}$ ,  $a = 55 \text{ nm}$ , we obtain  $\zeta_0 a^3/U_0 \approx 4.058 \mu\text{sec}$ . This yields for  $b = 44 \text{ nm}$  and  $n = 5$ ,  $\tau_{sc} \approx 0.404 \text{ msec}$ , and for  $n = 7$ ,  $\tau_{sc} \approx 0.905 \text{ msec}$ .

- 
- [1] S. J. Webb and D. D. Dodds, *Nature (London)* **218**, 374 (1968).  
 [2] N. D. Devyatkov, *Sov. Phys. Usp.* **16**, 568 (1974).

- [3] W. Grundler and F. Keilmann, *Phys. Rev. Lett.* **51**, 1214 (1983).  
 [4] C. B. Grissom, *Chem. Rev.* **95**, 3 (1995).

- [5] V. N. Binh, *Magnetobiology: Underlying Physical Problems* (Academic Press, San Diego, 2002).
- [6] V. N. Binh and A. V. Savin, *Physics Uspekhi* **46**, 259 (2003).
- [7] N. D. Devyatkov, M. B. Golant, and O. V. Betsky, *Millimeter Waves and Their Role in Vital Processes* (Moscow, Radio and Svyaz, 1991) (in Russian).
- [8] *Handbook of Biological Effects of Electromagnetic Fields: Bioengineering and Biophysical Aspects of Electromagnetic Fields*, 3d edition, edited by F. S. Barnes and B. Greenebaum (Taylor & Francis, Boca Raton, 2006).
- [9] V. Pikov, X. Arakaki, M. Harrington, S. F. Fraser, and P. H. Siegel, *J. Neural Eng.* **7**, 045003 (2010).
- [10] *Magnetite Biomineralization and Magnetoreception in Organisms: a New Biomagnetism*, edited by J. L. Kirschvink, D. S. Jones, and B. J. MacFadden (Plenum Press, New York, 1985).
- [11] J. L. Kirschvink and J. L. Gould, *Biosystems* **13**, 181 (1981).
- [12] J. L. Kirschvink, *Phys. Rev. A* **46**, 2178 (1992).
- [13] W. Wiltshko and R. Wiltshko, *J. Comp. Physiol. A* **191**, 675 (2005).
- [14] K. Schulten, C. E. Swenberg, and A. Weller, *Z. Phys. Chem.* **111**, 1 (1978); T. Ritz, S. Adem, and K. Schulten, *Biophys. J.* **78**, 707 (2000); C. T. Rodgers and P. J. Hore, *Proc. Natl. Acad. Sci. USA* **106**, 353 (2009).
- [15] R. K. Adair, *Phys. Rev. A* **43**, 1039 (1991); *Proc. Natl. Acad. Sci. USA* **91**, 2925 (1994).
- [16] R. Blakemore, *Science* **190**, 377 (1975).
- [17] D. Faivre and D. Schüler, *Chem. Rev.* **108**, 4875 (2008).
- [18] B. Devouard, M. Posfai, X. Hua, D. Bazylinski, R. B. Frankel, and P. R. Buseck, *Amer. Mineralogist* **83**, 1387 (1998).
- [19] L. G. Abracado, F. Abreu, C. N. Keim, A. P. C. Campos, U. Lins, and M. Farina, *Phys. Biol.* **7**, 046016 (2010).
- [20] J. L. Kirschvink, A. Kobayashi-Kirschvink, and B. J. Woodford, *Proc. Natl. Acad. Sci. USA* **89**, 7683 (1992).
- [21] S. H. K. Eder, H. Cadiou, A. Muhamad, P. A. McNaughton, J. L. Kirschvink, and M. Winklhofer, *Proc. Natl. Acad. Sci. USA* **109**, 12022 (2012).
- [22] N. B. Edelman, *et al.*, *Proc. Natl. Acad. Sci. USA* **112**, 262 (2015).
- [23] J. Dobson, *Exp. Brain Res.* **144**, 122 (2002).
- [24] V. N. Binh and D. S. Chernavskii, *Europhys. Lett.* **70**, 850 (2005); V. N. Binh, *Bioelectromagnetics* **27**, 58 (2006); V. N. Binh, *Int. J. Rad. Biol.* **84**, 569 (2008).
- [25] J. Vanderstaeten and P. Gillis, *Bioelectromagnetics* **31**, 371 (2010).
- [26] V. P. Shcherbakov, M. Winklhofer, M. Hanzlik, N. Petersen, *Eur. Biophys. J.* **26**, 319 (1997).
- [27] A. Körnig, J. Dong, M. Bennet, M. Widdrat, J. Andert, F. D. Müller, D. Schüler, S. Klumpp, and D. Faivre, *Nanoletters* **14**, 4653 (2014).
- [28] E. D. Yorke, *J. Theor. Biol.* **77**, 101 (1979).
- [29] M. Winklhofer and J. L. Kirschvink, *J. R. Soc. Interface* **7**, S273 (2010).
- [30] L. Yan and S. Tao, *Chin. Phys. B* **22**, 048701 (2013).
- [31] D. Mohanta, E. Stava, M. Yu, and R. H. Blick, *Phys. Rev. E* **89**, 012707 (2014).
- [32] S. M. Bezrukov, R. P. Rand, I. Vodyanoy, and V. A. Parsegian, *Faraday Discuss.* **111**, 173 (1998).
- [33] M. B. Jackson, *Molecular and Cellular Biophysics* (Cambridge University Press, Cambridge, 2006).
- [34] J. Howard and A. J. Hudspeth, *Neuron* **1**, 189 (1988); A. J. Hudspeth, Y. Choe, A. D. Mehta, and P. Martin, *Proc. Natl. Acad. Sci. USA* **97**, 11765 (2000).
- [35] L. S. Liebovitch and J. M. Sullivan, *Biophys. J.* **52**, 979 (1987).
- [36] T. L. Croxton, *Biochim. Biophys. Acta* **946**, 19 (1988).
- [37] P. Läuger, *Biophys. J.* **53**, 877 (1988).
- [38] G. L. Millhauser, E. E. Salpeter, R. E. Oswald, *Proc. Natl. Acad. Sci. USA* **85**, 1503 (1988).
- [39] M. S. P. Sansom, F. G. Ball, C. J. Kerry, R. McGee, R. L. Ramsey, and P. N. R. Usherwood, *Biophys. J.* **56**, 1229 (1989).
- [40] E. Gorczynska, P. L. Huddie, B. A. Miller, I. R. Mellor, H. Vais, R. K. Ramsey, and P. N. R. Usherwood, *Pfluegers Arch.* **432**, 597 (1996); S. Mercik and K. Weron, *Phys. Rev. E* **63**, 051910 (2001).
- [41] Z. Qu, G. Hu, A. Garfinkel, J. N. Weiss, *Phys. Rep.* **543**, 61 (2014).
- [42] R. H. Austin, K. Beeson, L. Eisenstein, H. Frauenfelder, I. C. Gunsalus, and V. P. Marshall, *Phys. Rev. Lett.* **32**, 403 (1974).
- [43] H. Frauenfelder, S. G. Sligar, and P. G. Wolynes, *Science* **254**, 1598 (1991); H. Frauenfelder, P. W. Fenimore, G. Chen, and B. H. McMahon, *Proc. Natl. Acad. Sci. USA* **103**, 15469 (2006); H. Frauenfelder, *et al.*, *Proc. Natl. Acad. Sci. USA* **106**, 5129 (2006).
- [44] S. M. Rappaport, O. Teijido, D. P. Hoogerheide, T. K. Rostovtseva, A. M. Berezhkovskii, and S. M. Bezrukov, *Eur. Biophys. J.* **44**, 465 (2015).
- [45] I. Goychuk and P. Hänggi, *Proc. Natl. Acad. Sci. USA* **99**, 3552 (2002); *Physica A* **325**, 9 (2003).
- [46] I. Goychuk and P. Hänggi, *Phys. Rev. E* **70**, 051915 (2004).
- [47] I. Goychuk, *Phys. Rev. E* **80**, 046125 (2009).
- [48] I. Goychuk, *Adv. Chem. Phys.* **150**, 187 (2012).
- [49] J.-H. Jeon, H. M.-S. Monne, M. Javanainen, and R. Metzler, *Phys. Rev. Lett.* **109**, 188103 (2012).
- [50] T. G. Mason and D. A. Weitz, *Phys. Rev. Lett.* **74**, 1250 (1995).
- [51] F. Amblard, A. C. Maggs, B. Yurke, A. N. Pargellis, and S. Leibler, *Phys. Rev. Lett.* **77**, 4470 (1996).
- [52] A. Caspi, R. Granek, and M. Elbaum, *Phys. Rev. E* **66**, 011916 (2002).
- [53] D. Mizuno, C. Tardin, C. F. Schmidt, and F. C. MacKintosh, *Science* **315**, 370 (2007).
- [54] T. A. Waigh, *Rep. Prog. Phys.* **68**, 685 (2005).
- [55] J. Szymanski and M. Weiss, *Phys. Rev. Lett.* **103**, 038102 (2009).
- [56] I. Santamaria-Holek, J. M. Rubi, and A. Gadomski, *J. Phys. Chem. B* **111**, 2293 (2007).
- [57] G. Guigas, C. Kalla, and M. Weiss, *Biophys. J.* **93**, 316 (2007); M. Weiss, *Phys. Rev. E* **88**, 010101 (2013).
- [58] S. C. Weber, A. J. Spakowitz, J. A. Theriot, *Phys. Rev. Lett.* **104**, 238102 (2010).
- [59] C. Wilhelm, *Phys. Rev. Lett.* **101**, 028101 (2008); D. Robert, Th.-H. Nguyen, F. Gallet, and C. Wilhelm, *PLoS ONE* **4**, e10046 (2010).
- [60] L. Bruno, M. Salierno, D. E. Wetzler, M. A. Desposito, V. Levi, *PLoS ONE* **6**, e18332 (2011).
- [61] S. C. Kou and X. S. Xie, *Phys. Rev. Lett.* **93**, 180603 (2004).
- [62] S. A. Adelman, *J. Chem. Phys.* **64**, 124 (1976); P. Hänggi and H. Thomas, *Z. Phys. B* **26**, 85 (1977); P. Hänggi, H. Thomas, H. Grabert, and P. Talkner, *J. Stat.*

- Phys. **18**, 155 (1978); P. Hänggi, Z. Phys. B **31**, 407 (1978).
- [63] I. Goychuk and P. Hänggi, Phys. Rev. Lett. **99**, 200601 (2007).
- [64] P. Siegle, I. Goychuk, P. Talkner, and P. Hänggi, Phys. Rev. E **81**, 011136 (2010); P. Siegle, I. Goychuk, and P. Hänggi, Phys. Rev. Lett. **105**, 100602 (2010); P. Siegle, I. Goychuk, and P. Hänggi, Europhys. Lett. **93**, 20002 (2011).
- [65] I. Goychuk and P. Hänggi, in *Fractional Dynamics: Recent Advances*, edited by J. Klafter, S. C. Lim, and R. Metzler (World Scientific, Singapore, 2011), Chap. 13, pp. 307-329.
- [66] I. Goychuk, Chem. Phys. **375**, 450 (2010).
- [67] I. Goychuk and V. Kharchenko, Phys. Rev. E **85**, 051131 (2012).
- [68] I. Goychuk and V. Kharchenko, Math. Model. Nat. Phenom. **8**, 144 (2013).
- [69] V. O. Kharchenko and I. Goychuk, Phys. Rev. E **87**, 052119 (2013).
- [70] V. Kharchenko and I. Goychuk, New J. Phys. **14**, 043042 (2012).
- [71] I. Goychuk, V.O. Kharchenko and R. Metzler, PLoS ONE **9**, e91700 (2014).
- [72] I. Goychuk, V.O. Kharchenko and R. Metzler, Phys. Chem. Chem. Phys. **16**, 16524 (2014).
- [73] I. Goychuk, Phys. Biol. **12**, 016013 (2015).
- [74] K. Luby-Phelps, Mol. Biol. Cell **24**, 2593 (2013).
- [75] I. Goychuk, Phys. Rev. E **86**, 021113 (2012).
- [76] T. Odijk, Biophys. J. **79**, 2314 (2000); L. Masaro and X. X. Zhu, Prog. Polym. Sci. **24**, 731 (1999); R. Holyst, *et al.*, Phys. Chem. Chem. Phys. **11**, 9025 (2009).
- [77] B. R. Parry, I. V. Surovtsev, M. T. Cabeen, C. S. O'Hern, E. R. Dufresne, C. Jacobs-Wagner, Cell **156**, 183 (2014).
- [78] H. A. Kramers, Physica (Utrecht) **7**, 284 (1940).
- [79] R. F. Grote and J. T. Hynes, J. Chem. Phys. **73**, 2715 (1980).
- [80] P. Hänggi and F. Mojtabai, Phys. Rev. A **26**, 1168 (1982).
- [81] B. Carmeli and A. Nitzan, J. Chem. Phys. **79**, 393 (1983).
- [82] E. Pollak, H. Grabert, and P. Hänggi, J. Chem. Phys. **91**, 4073 (1989).
- [83] P. Hänggi, P. Talkner, and B. Borkovec, Rev. Mod. Phys. **62**, 251 (1990).
- [84] I. Goychuk, Fluct. Noise Lett. **11**, 1240009 (2012).
- [85] I. Goychuk and V. O. Kharchenko, Phys. Rev. Lett. **113**, 100601 (2014).
- [86] M. Herrchen and H. C. Öttinger, J. Non-Newtonian Fluid Mech., **68**, 17 (1997).
- [87] H. Kojima, E. Muto, H. Higuchi and T. Yanagida, Biophys. J. **73**, 2012 (1996).
- [88] Ch. Koch, *Biophysics of Computation: Information Processing in Single Neurons* (Oxford University Press, New York, 1999).
- [89] R. Kubo, Rep. Prog. Phys. **29**, 255 (1966); R. Kubo, M. Toda, and M. Hashitsume, *Nonequilibrium Statistical Mechanics*, 2nd ed. (Springer, Berlin, 1991).
- [90] G. W. Ford, M. Kac, and P. Mazur, J. Math. Phys. **6**, 504 (1965); G. W. Ford, J. T. Lewis, and R. F. O'Connell, Phys. Rev. A **37**, 4419 (1988).
- [91] R. Zwanzig, *Nonequilibrium Statistical Mechanics* (Oxford University Press, Oxford, 2001).
- [92] W. T. Coffey and Y. P. Kalmykov, *The Langevin Equation, With Applications to Stochastic Problems in Physics, Chemistry and Electrical Engineering*, 3d ed. (World Scientific, New Jersey, 2012).
- [93] A. Gemant, Physics **7**, 311 (1936).
- [94] W. B. Russel, D. A. Saville, and W. R. Schowalter, *Colloidal Dispersions* (Cambridge University Press, Cambridge, 1989).
- [95] R. Metzler and J. Klafter, Phys. Rep. **339**, 1 (2000).
- [96] F. Mainardi and P. Pironi, Extracta Mathematicae **11**, 140 (1996).
- [97] E. Lutz, Phys. Rev. E **64**, 051106 (2001).
- [98] U. Weiss, *Quantum Dissipative Systems*, 2nd ed. (World Scientific, Singapore, 1999).
- [99] I. Goychuk, Phys. Rev. E **76**, 040102(R) (2007).
- [100] J. H. P. Schulz, E. Barkai, and R. Metzler, Phys. Rev. X **4**, 011028 (2014).
- [101] I. Goychuk, Commun. Theor. Phys. **62**, 497 (2014).
- [102] H. Stehfest, Comm. ACM **13**, 47 (1970); H. Stehfest, Comm. ACM **13**, 624 (1970)(Erratum).
- [103] I. Goychuk and P. Hänggi, Chem. Phys. **324**, 160 (2006).
- [104] J. N. Israelachvili, *Intermolecular and Surface Forces*, 3d ed. (Academic Press, Waltham, 2011).
- [105] T. D. Pollard, W. C. Earnshaw, J. Lippincott-Schwartz, *Cell Biology*, 2nd ed. (Saunders Elsevier, Philadelphia, 2007).
- [106] B. C. Arnold, *Pareto Distributions*, 2nd ed. (CRC Press, Boca Raton, 2015).
- [107] See Supplemental Material below.
- [108] The choice  $p_1 = p_2$  is not appropriate because given an ideal time resolution of current recordings one would detect many false open-shut transitions corresponding to erratic fluctuations (fast recrossings) around the threshold value  $\phi_{th}$  solving  $p_1(\phi_{th}) = p_2(\phi_{th}) = 0.5$ . Such fast recrossings simply do not correspond to transitions between two macrostate.
- [109] J. D. Jackson, *Classical Electrodynamics*, 3d ed. (John Wiley, New York, 1999).
- [110] J. Garcia de la Torre and V. Bloomfield, Q. Rev. Biophys. **14**, 81 (1981).

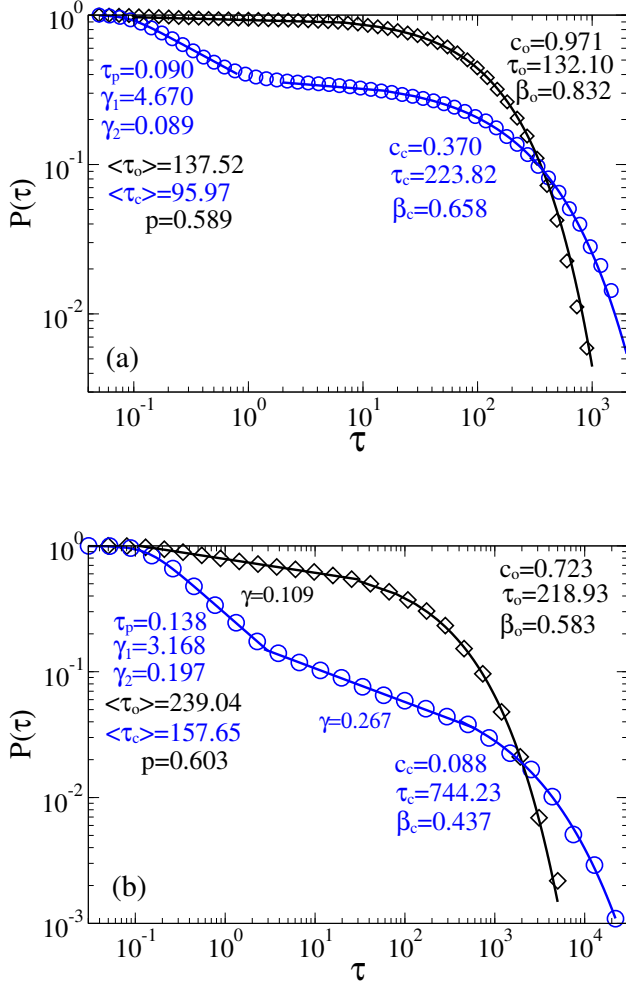


FIG. 12. Survival probabilities of open (black diamond symbols), and closed (blue open circles) times derived from numerical data for the case  $\mu B = 0.3115$ ,  $\psi = \pi$ , using the detection thresholds  $p_1 = 0.2$ ,  $p_2 = 0.7$  for (a)  $\eta_{\text{eff}} = 100$ , and (b)  $\eta_{\text{eff}} = 1000$ . Lines present the corresponding stretched exponential,  $c_i \exp[-(\tau/\tau_i)^{\beta_i}]$ , Pareto law (24), and power law,  $\sim \tau^{-\gamma}$ , fits with the parameters shown in the plots. The mean residence times, as well as the opening probability defined as a time average  $p = \langle \tau_o \rangle / (\langle \tau_o \rangle + \langle \tau_c \rangle)$  are also displayed. Other parameters:  $T = 0.1$ ,  $l_{\text{max}} = 1.5$ ,  $f_0 = 1.5$ ,  $l_0 = 1.22$ , and  $m = 7$  channels in the sensor cluster.

## Supplemental Material

### Influence of different thresholds on statistics of fluctuations in non-Markovian case.

Here, we present the results of simulations of the same non-Markovian stochastic dynamics, which is discussed in relation to Figs. 8, 9 of the main text, for two additional choices of thresholds. These are the same as in Figs. 6 (a), (b) of the main text. For the thresholds set at

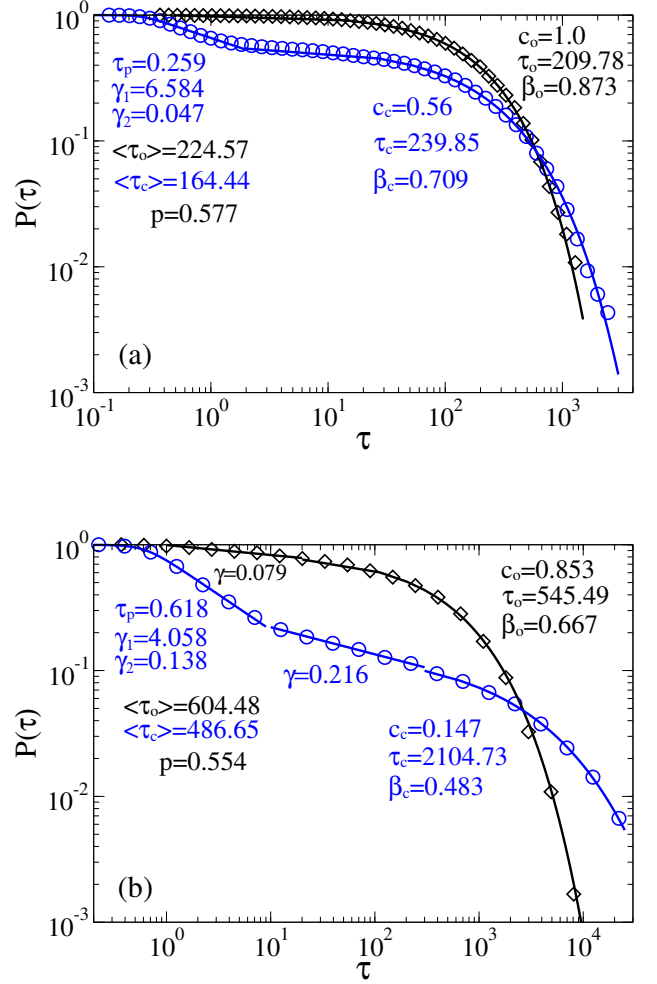


FIG. 13. Survival probabilities of open (black diamond symbols), and closed (blue open circles) times derived from numerical data for the case  $\mu B = 0.3115$ ,  $\psi = \pi$ , using the detection thresholds  $p_1 = 0.1$ ,  $p_2 = 0.9$  for (a)  $\eta_{\text{eff}} = 100$ , and (b)  $\eta_{\text{eff}} = 1000$ . Lines present the corresponding stretched exponential,  $c_i \exp[-(\tau/\tau_i)^{\beta_i}]$ , Pareto law (24), and power law,  $\sim \tau^{-\gamma}$ , fits with the parameters shown in the plots. The mean residence times, as well as the opening probability defined as a time average  $p = \langle \tau_o \rangle / (\langle \tau_o \rangle + \langle \tau_c \rangle)$  are also displayed. Other parameters:  $T = 0.1$ ,  $l_{\text{max}} = 1.5$ ,  $f_0 = 1.5$ ,  $l_0 = 1.22$ , and  $m = 7$  channels in the sensor cluster.

$p_1 = 0.2$ ,  $p_2 = 0.7$  and  $\eta_{\text{eff}} = 100$ , see in Fig. 12 (a), the distribution of open time is almost single stretched exponential ( $c_o \approx 0.97$ ) with  $\beta_o \approx 0.83$ , and the tail of the closed time distribution is a stretched exponential with  $\beta_c \approx 0.66$ . Notice that the time constants  $\tau_o$  and  $\tau_c$ , as well as the weight  $c_c$  changed a little, as compare with the corresponding Markovian case in Fig. 6 (a) of the main text. Almost 50% of initial closed time kinetics follows a power law with  $\gamma = \gamma_1 \gamma_2 \approx 0.416$ . It corresponds to a power law residence time distribution,  $\psi_c(\tau) \propto \tau^{-\delta}$ , with  $\delta = 1 + \gamma \approx 1.416$ , which is not changed essentially

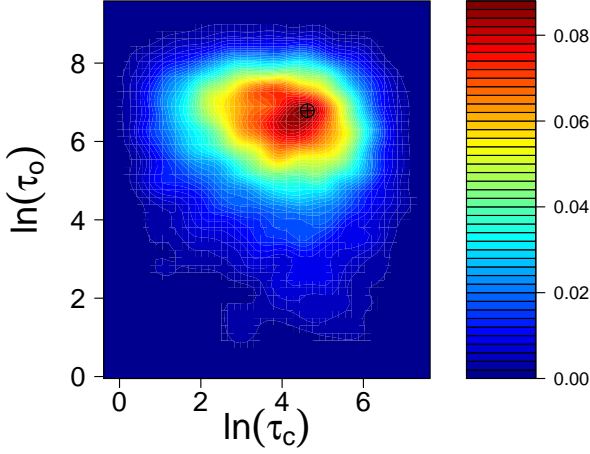


FIG. 14. Two-dimensional density of logarithmically transformed closed,  $\ln \tau_c$ , and open,  $\ln \tau_o$ , residence times, derived from numerical data for the case  $\mu B = 0.4363$ ,  $\psi = \pi$ , using the detection thresholds defined by the minima of  $U(\phi)$  for  $\eta_{\text{eff}} = 100$ . The corresponding survival probabilities of residence times are depicted in Fig. 11 (a) (main text). The symbol represents the result of NMRT with the approximate memory kernel. It agrees well with the most probable values of the log-transformed times.

from one which follows from the results in Fig. 6 (a) of the main text, i.e.  $\delta \approx 1.424$ . The mean residence times changed also insignificantly, very differently from what to expect from a trivial renormalization of the normal friction by the factor of 100. This is a very important result. Notice also that these results correspond in fact to a fixed value  $\eta_\alpha$  and will not be changed significantly if to increase  $\tau_h$  by increasing the number of auxiliary Brownian particles representing environment in simulations and increasing at the same time  $\eta_{\text{eff}}$ , so that  $\eta_\alpha$  remains the same, see the main text. Hence, the sensor can operate equally well even for much larger  $\eta_{\text{eff}}$ . The increase of  $\eta_\alpha$  can, however, essentially modify the results, see in Fig. 12 (b), for  $\eta_{\text{eff}} = 1000$ , with other parameters kept the same. Indeed, let us consider the distribution of closed times in this figure. First, initial Pareto law becomes different with  $\gamma = \gamma_1 \gamma_2 \approx 0.624$ , compare with  $\gamma = \gamma_1 \gamma_2 \approx 0.418$  in Fig. 12 (a). Second, it is followed now by a novel intermediate power law with  $\gamma \approx 0.267$ . Third, the stretched exponential tail has very different parameters  $\tau_c$  and  $\beta_c$ . Also the distribution of open times becomes strongly affected. Namely, it displays an intermediate power law with  $\gamma \approx 0.109$ , and also  $\beta_o$  becomes essentially smaller and  $\tau_o$  larger.

If to change the detection thresholds to  $p_1 = 0.1$  and  $p_2 = 0.9$ , the results depicted in Fig. 13 are got modified. In particular, for  $\tilde{\eta}_{\text{eff}} = 100$  in Fig. 13 (a), the initial

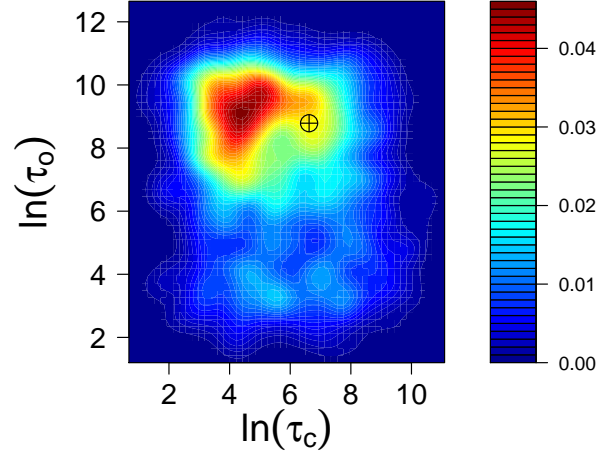


FIG. 15. Two-dimensional density of logarithmically transformed closed,  $\ln \tau_c$ , and open,  $\ln \tau_o$ , residence times, derived from numerical data for the case  $\mu B = 0.4363$ ,  $\psi = \pi$ , using the detection thresholds defined by the minima of  $U(\phi)$  for  $\eta_{\text{eff}} = 1000$ . The corresponding survival probabilities of residence times are depicted in Fig. 11 (b) (main text). The symbol represents the result of NMRT with the approximate memory kernel. It clearly does not fit to the most probable  $\ln \tau_c$ . The agreement with  $\ln \tau_o$  is better. This is because the potential barrier to leave the second (open conformation) potential well is much higher than one in the first (closed conformation) potential well. However, the agreement with  $\ln \tau_o$  is also much worse than in Fig. 14. This is because the approximation by a single stretched exponential in Fig. 11 (b) is not good for closed times.

power law of closed times is changed to  $\gamma = \gamma_1 \gamma_2 \approx 0.309$ . The stretched exponential parameters  $\beta_o$  and  $\beta_c$ ,  $\tau_o$  and  $\tau_c$  are changed also. Also for  $\tilde{\eta}_{\text{eff}} = 1000$  in Fig. 13 (b), the changes are evident: initial power law of closed times becomes  $\gamma = \gamma_1 \gamma_2 \approx 0.560$  and also intermediate power law of closed times is changed, compare Fig. 13 (b) with Fig. 12 (b). The changes occur also in the weights and other parameters of stretched exponential tails of both closed and open times survival probabilities.

#### Two-dimensional densities corresponding to Fig. 11 of the main text.

Figs. 14 and 15 present two-dimensional probability density plots corresponding to Fig. 11 (a), and Fig. 11 (b) of the main text, respectively, and provide some important additional insight. Indeed, in Fig. 14 a good agreement between  $\ln \tau_o^{(\text{NMRT})}$  and most probable  $\ln \tau_o$ , as well as between  $\ln \tau_c^{(\text{NMRT})}$  and most probable  $\ln \tau_c$  is evident. In this case, a single stretched exponential



fit used in Fig. 11 (a) is also good. However, in Fig. 15,  $\ln \tau_c^{(\text{NMRT})}$  strongly disagrees with the most probable  $\ln \tau_c$ , and a single exponential fit in Fig. 11 (b) simply fails for the closed time distribution. The agreement between  $\ln \tau_o^{(\text{NMRT})}$  and the most probable  $\ln \tau_o$  is not bad. This is because the barrier is essentially larger in this case. Indeed, the agreement with NMRT can be ex-

pected only for sufficiently large barriers with  $\beta_i$  close to one. However, it also seems worse than the analysis related to Fig. 11 (b) suggests. This is because the approximation of single stretched exponential used in Fig. 11 (b) is also not very good for the open times. Yet it is really astonishing that NMRT is of a good predictive value for  $\ln \tau_o$  even here and in Fig. 11 (b), for  $\beta_o \approx 0.549$ .